A flexible genuinely nonlinear approach for wave propagation, breaking and runup

Andrea Gilberto Filippini, Maria Kazolea, Mario Ricchiuto

A flexible genuinely nonlinear approach for wave propagation, breaking and runup

A.G. Filippini, M. Kazolea , M. Ricchiuto

RESEARCH REPORT
N° 8746
June 2015
Project-Teams CARDAMOM

ISSN 0249-6399 ISRN INRIA/RR--8746--FR+ENG

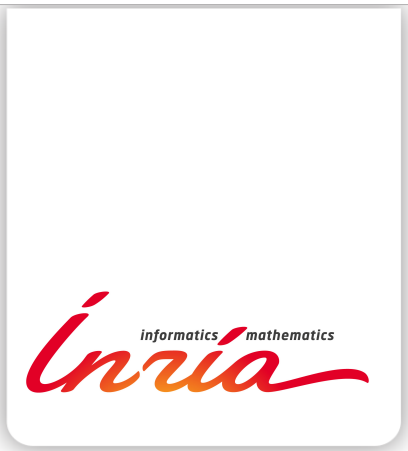

A flexible genuinely nonlinear approach for wave propagation, breaking and runup

A.G. Filippini *, M. Kazolea *, M. Ricchiuto†

Project-Teams CARDAMOM

Research Report n° 8746 — June 2015 — 56 pages

Abstract: In this paper we evaluate hybrid strategies for the solution of the Green-Nagdhi system of equations for the simulation of fully nonlinear and weakly dispersive free surface waves. We consider a two steps solution procedure composed by: a first step where the non hydrostatic source term is recovered by inverting the elliptic coercive operator associated to the dispersive effects; a second step which involves the solution of the hyperbolic shallow water system with the source term, computed in the previous phase, which accounts for the non-hydrostatic effects. Appropriate numerical methods that can be also generalized on arbitrary unstructured meshes are used to discretize the two stages: the standard C^0 Galerkin finite element method for the elliptic phase; either third order Finite Volume of third order stabilized Finite Element methods for the hyperbolic phase. The discrete dispersion properties of the fully coupled schemes obtained are studied, showing accuracy close or better to that of a fourth order finite difference method. The hybrid approach of locally reverting to the nonlinear shallow water equations is used to recover energy dissipation in breaking regions. To this scope we evaluate two strategies : simply neglecting the non-hydrostatic contribution in the hyperbolic phase ; imposing a tighter coupling of the two phases, with a wave breaking indicator embedded in the elliptic phase to smoothly turn off the dispersive effects. The discrete models obtained are thoroughly tested on benchmarks involving wave dispersion, breaking and runup, showing a very promising potential for the simulation of complex near shore wave physics in terms of accuracy and robustness.

Key-words: Green-Nagdi equations, Wave breaking, Finite Volumes, Finite Elements, hybrid scheme

* Inria BSO, Team CARDAMOM
† sfn

RESEARCH CENTRE
BORDEAUX – SUD-OUEST

351, Cours de la Libération
Bâtiment A 29
33405 Talence Cedex

A flexible genuinely nonlinear approach for wave propagation, breaking and runup

Résumé : Dans cet article on étudie des strategies hybrides pour la simulation numérique d'ondes de surface en regime fully-nonlinear/weakly-dispersive. On évalue une procedure de resolution des équations de type Green-Naghdi bassée sur deux étapes: un premiere étape dans laquelle l'opérateur elliptique associé aux effects dispersifs est inversé par une méthode élélements finis ; une deuxiéme étape hyperbolique dans laquelle les quantités physiques sont évolués en résolvant les equations shallow water avec des méthodes de type shock capturing. Les schémas choisis pour les deux étapes sont de type volumes et éléments finis dont une généralisation au cas multi-dimensionnel sur maillages non-stucturée existe déjà. L'erreurs de dispersion des méthodes hybrides ainsi obtenues est étudiés en detail, en montrant qu'un precision treѕ proche de celle d'une méthode différence finies d'ordre quatre peut être obtenue. Pour gérer le dférlement, on utilise un approche hybride basé sulr la rsolution locale des equation shallow water. Deux stratégies de couplage sont proposées et testés numériquement. Les résultats montrent qu'un couplage plus fort entre la phase elliptique et la phase hyperbolique permet un passage plus lisse entre les régions déférlantes et non-déférlantes. Une validation sur de nombreux cas test montre le potentiel de l'approche proposée.

Mots-clés : Green-Nagdi equations, Wave breaking, Finite Volumes, Finite Elements, hybrid scheme

Contents

1 Introduction

The accurate mathematical and numerical simulation of water wave propagation in near-shore regions have received considerable attention in the last decades, since they have largely replaced laboratory experiments in the coastal engineering community. Significant efforts have been made in the development of depth averaged models or in the improvement of the existing ones, in order to give accurate description to the nonlinear and non-hydrostatic propagation over complex bathymetries.

The use of asymptotic depth averaged models or this task is quite common since they lead to numerical models that are of practical use in design compared to the ones produced by more complicated mathematical models like the Euler

equations. One of the most known depth averaged models, widely used, are the non linear shallow water equations (NLSW). This set of equations are capable of providing a good description of the non-linear transformation of the waves, including also wave breaking but they lack on describing all the dispersive effects that play an important role on deeper waters and on wave shoaling. As to take in to account the dispersion effects the use of asymptotic depth averaged Boussinesq and enhanced Boussinesq [40, 34, 32, 6, 61] type models is quite common. A review on the history and all the fundamental aspects of the Boussinesq-type models can be found in [10].

The last decades a system of equations produced by the Euler equations have gained a lot of attention. Green and Nagdi [20] derived a fully non-linear weakly dispersive set of equations for an uneven bottom which represents a two dimensional extension of the Serre equations [49]. They are known as Serre or Green-Naghdi (GN) , or fully non-linear Boussinesq equations. The range of validity of the model may vary as much as far the non-linearity parameter (ϵ) is concerned but it requires that the shallowness parameter (μ) to be small (less than one). The GN model has been fully justified mathematically [**?**] in the sense that the error between the solutions of the GN system and the Euler equations is small and of size $O(\mu^2)$. We refer to [28, 8] for more details.

From the numerical point of view the GN equations have been discretized using different numerical techniques like Finite Differences (FD), Finite Elements (FE) and Finite Volume (FV) approaches. We refer to [1, 15, 16, 14, 8, 35, 30, 36, **?**] among others . For example the authors in [15, 16] derive a higher order FV scheme in one dimension. In [14, 8] a hybrid FV/FD splitting approach is used while [35] follows the same idea for the solution of a new class of two-dimensional GN equations on structured meshes. In [30] a coupled discontinuous Galerkin and Continuous Galerkin is developed in one dimension but using only flat bottom topographies. Most of them are also really hard to extend in two dimensions. Up to now and to the authors knowledge there is no work that involves the solution of the later equations in 2D unstructured meshes.

Like all the Boussinesq-type models, GN eqautions can produce satisfactory results only for the waves before wave breaking. For this reason the numerical model must be incorporated with a wave breaking mechanism as to handle broken waves. Several approaches wave been developed among the years. An extensive review of the existing wave breaking techniques can be found in [25].

In this work our first aim is to evaluate a strategy that can be easily generalized on arbitrary unstructured meshes in the multidimensional case for the solution of fully nonlinear, weakly dispersive free surface waves. For this reason we consider the hybrid approach, used e.g. in [8] and [25] using Green-Nagdhi partial differential equations (PDEs) for propagation and shoaling, while locally reverting to the non-linear shallow water equations to model energy dissipation in breaking regions. Starting from the form of the Green-Nagdi equations proposed in [8] and [14], we consider a two steps solution procedure : an elliptic phase in which a source term is computed by inverting the coercive operator associated to the dispersive effects ; an hyperbolic phase in which the flow variables are evolved by solving the nonlinear shallow water equations, with all non-hydrostatic effects accounted for by the source computed in the elliptic phase. For the numerical discretization of these two steps we consider methods which can be easily generalized on arbitrary unstructured meshes in the multi-

dimensional case. In particular, we focus on the use of a standard C^0 Galerkin finite element method for the elliptic phase, while high order finite volume (FV) and stabilized finite element (FE) methods are used independently in the hyperbolic phase. The discrete dispersion properties of the fully coupled methods thus obtained are studied showing phase accuracy very close to that of a fourth order finite difference method.

In addition, we will exploit the two steps solution procedure to obtain a robust embedding of wave breaking We evaluate two strategies : one based on simply neglecting the non-hydrostatic contribution in the hyperbolic phase ; the second involving a tighter coupling of the two phases, with a wave breaking indicator embedded in the elliptic phase to smoothly turn off the dispersive effects. The discrete models obtained are thoroughly tested on benchmarks involving wave dispersion, breaking and runup, showing a very promising potential for the simulation of complex near shore wave physics.

The paper is organized as follows: The second section describes the mathematical model and the notation used in this work. Then, the equations are re-written obtaining an elliptic-hyperbolic decoupling and the details of two discretization strategies are presented. Section four completes the description of the basic discretizations with a discussion of the time integration schemes along with boundary condition treatment and friction. In section five, the dispersion behaviour of both the spatial and temporal discretizations is analyzed in detail, while two alternative ways of embedding wave breaking are proposed in section six. Finally, in section seven the performance of the proposed methodology is extensively validated against experimental measurements from a series of relevant benchmark problems.

2 The physical model

In this work we refer to the improved Green-Nagdi (GN) system of equations in the form proposed by [8]. This formulation has been recovered by adding some terms of $O(\mu^2)$ to the momentum equation in order to improve the frequency dispersion description of the original GN model. In the following we use the notation sketched in figure 1, thus we denote $h(x,t) = h_0 + \eta(x,t) - b(x)$ the total water depth (being $\eta(x,t)$ the free surface elevation with respect to the water's rest state, h_0 a reference depth and $b(x)$ the topography variation) and $u(x,t)$ the flow velocity.

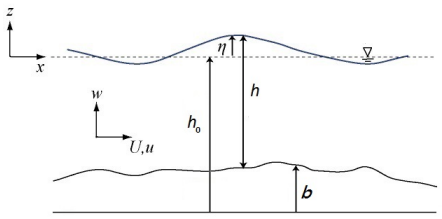

Figure 1: Sketch of the free surface flow problem, main parameter description.

The one-dimensional system of equation (derived from [8]) can thus be writ-

ten in its one-dimensional form as:

$$\begin{aligned} h_t + (hu)_x &= 0 \qquad (1)\\ (I+\alpha\mathcal{T})\left[(hu)_t + (hu^2)_x + g\frac{\alpha-1}{\alpha}h\eta_x\right] + \frac{g}{\alpha}h\eta_x + h\mathcal{Q}(u) &= 0 \end{aligned}$$

where $\mathcal{T}(\cdot)$ and $\mathcal{Q}(\cdot)$ are the linear operators:

$$\mathcal{T}(\cdot) = -\frac{1}{3}h^2(\cdot)_{xx} - \frac{1}{3}hh_x(\cdot)_x + \frac{1}{3}\left[h_x^2 + hh_{xx}\right](\cdot) + \left[b_xh_x + \frac{1}{2}hb_{xx} + b_x^2\right](\cdot) \qquad (2)$$

$$\mathcal{Q}(\cdot) = 2hh_x(\cdot)_x^2 + \frac{4}{3}h^2(\cdot)_x(\cdot)_{xx} + b_xh(\cdot)_x^2 + b_{xx}h(\cdot)(\cdot)_x + \left[b_{xx}h_x + \frac{1}{2}hb_{xxx} + b_xb_{xx}\right](\cdot) \qquad (3)$$

α is a parameter which is used to improve the dispersion properties of the model in order to obtain a good matching with respect to the linearized full Euler equations. The linear dispersion relation of this model can be recovered in the very classical way [33] by introducing in the linearized version of system (1) a solution $W = [h, hu]^T$ expressed in the form of a Fourier mode $W = W_0 \exp^{\nu t + jkx}$ with $\nu = \xi + j\omega$, ω denoting the phase of the mode, ξ representing the rate of amplification/damping and k representing the wavenumber of the Fourier mode. The following dispersion relation can be found in this way:

$$\omega^2 = gh_0k^2\frac{1+\frac{\alpha-1}{3}k^2h_0^2}{1+\frac{\alpha}{3}k^2h_0^2}. \qquad (4)$$

Following [35], the value of the parameter α which optimizes the above relation is $\alpha = 1.159$, while the system (1) recover the classical GN equations when $\alpha = 1$. According to [35] the above formulation does not require the computation of third order derivatives, while this is necessary in the standard formulation of the GN system. Moreover, the presence of the operator $(I + \alpha\mathcal{T})$ makes the model very stable with respect to high frequency perturbations, which is of highest interest for numerical computations.

3 Discretization strategy : elliptic-hyperbolic decoupling

To discretize system (1) we recast it in the following way:

$$\begin{aligned} h_t + (hu)_x &= 0 \qquad (5)\\ (I+\alpha\mathcal{T})\left[(hu)_t + (hu^2)_x + gh\eta_x\right] - \mathcal{T}\left(gh\eta_x\right) + h\mathcal{Q}(u) &= 0 \end{aligned}$$

This allows the operator $(I + \alpha\mathcal{T})$ to be applied to the full shallow water residual. This form suggests a possible splitting of the elliptic part of the problem from the hyperbolic one, which is obtained as follow :

$$(I+\alpha\mathcal{T})\,\phi = \mathcal{W} - \mathcal{R} \qquad (6)$$

$$\begin{aligned} h_t + (hu)_x &= 0 \qquad (7)\\ (hu)_t + (hu^2)_x + gh\eta_x &= \phi \end{aligned}$$

having also defined $\mathcal{W} = g\mathcal{T}(h\eta_x)$ and $\mathcal{R} = h\mathcal{Q}(u)$. Given an initial solution, the system above can now be solved in two independent steps :

1. An elliptic step solving for the non-hydrostatic term ϕ ;
2. An hyperbolic step evolving the flow variables .

Our aim is to evaluate a strategy in which the two steps are each solved with an appropriate numerical method. In particular, in this paper we will focus on the use of a standard C^0 Galerkin finite element method for the elliptic phase, while high order finite volume (FV) and stabilized finite element (FE) methods are used independently in the hyperbolic phase. The resulting hybrid algorithms are compared. Other hybrid methods can be obtained by choosing different hyperbolic methods, such as e.g. the discontinous Galerkin method [64, 63], or the residual distribution method [42]. These different formulations will be discussed in the future. Here we will study the potential of a formulation which can be easily generalised on arbitrary unstructured meshes. In particular, we will consider the method obtained by only inverting in the elliptic phase the matrices obtained when considering a P^1 finite element approximation. As we will show, provided that a third order method is used in the hyperbolic phase, this choice already gives dispersion properties equivalent to those of a fourth order method. As we will see later, the additional advantage of this approach, is to allow a direct embedding of wave breaking either by simply neglecting the non-hydrostatic contribution in the hyperbolic phase, or even with a tighter coupling of the two phases using the breaking indicator to smoothly turn off ϕ in the elliptic phase.

The objective of the following sections is to discuss the methods used in this paper. The analysis of the dispersion error of the resulting scheme is then provided in section §5, while the treatment of wave breaking is discussed in section §6.

3.1 Spatial domain discretization and notation

Let $[0,\, L]$ be the spatial domain, we consider a tessellation composed of elements $[x_i,\, x_{i+1}]$. We set in general $\Delta x = \min_i(x_{i+1} - x_i)$. For simplicity we assume in the following that the points are equally spaced, so that $x_{i+1} - x_i = \Delta x$, but non-uniform meshes can be used with the same methods discussed here with very little modifications. For a given node i, we will denote by C_i the cell $[x_{i-1/2}\; x_{i+1/2}]$, with $x_{i+1/2} - x_{i-1/2} = \Delta x$.

On this mesh, we will denote by φ_i the standard hat shaped C^0 continuous Lagrange basis functions, and we will denote by $\mathbf{U}_{\Delta x}$ the piecewise continuous polynomial obtained as

$$\mathbf{U}_{\Delta x}(x,t) = \sum_i \varphi_i(x)\mathbf{U}_i(t)\,.$$

In this paper we consider the case of P^1 piecewise linear polynomials.

3.2 Elliptic phase : continuous finite element formulation

The first step for solving system (7) is to compute separately the value of the auxiliary variable ϕ from (6). In this work we discretize equation (6) by means of a standard C^0 Galerkin finite element approach. This discretization strategy passes by the writing of the variational form of the equation. The actual discretization is obtained by evaluating all the integrals by a numerical quadrature

over each element of the discretization, with the assumption of piecewise linear variation of all the quantities involved $h_{\Delta x},\ \eta_{\Delta x},\ b_{\Delta x},\ u_{\Delta x},\ \phi_{\Delta x}$. Defining $\Phi = [\phi_1(t),\ \phi_2(t),\ ...,\ \phi_N(t)]^T$ and $U = [u_1(t),\ u_2(t),\ ...,\ u_N(t)]^T$, the final form of the Galerkin approximation of the problem can be written as:

$$(\mathrm{M}^{\mathrm{G}} + \alpha \mathrm{T})\Phi = \mathrm{W} - \mathrm{R} \tag{8}$$

$$\mathrm{W} = \mathrm{T}\omega \tag{9}$$

$$\mathrm{R} = \mathrm{Q}U \tag{10}$$

Here M^{G} is the P^1 tridiagonal Galerkin mass matrix, whose general element is

$$\mathrm{M}^{\mathrm{G}}_{i,j} = \int_0^L \varphi_i \varphi_j \tag{11}$$

The matrices $\mathrm{T}(h_{\Delta x}, b_{\Delta x})$ and $\mathrm{Q}(h_{\Delta x}, b_{\Delta x}, \omega_{b\Delta x})$ are defined as follow (we will change the notation to indicate partial derivatives $\partial_{(\cdot)}$ for sake of clarity):

$$\begin{aligned}\mathrm{T}_{i,j}(h_{\Delta x}, b_{\Delta x}) = \ & \frac{1}{3}\int_0^L \partial_x\varphi_i\ h^2_{\Delta x}\ \partial_x\varphi_j\ -\ \frac{1}{3}\int_0^L \partial_x\varphi_i\ h_{\Delta x}\ \partial_x h_{\Delta x}\ \varphi_j\ + \\ & + \frac{1}{2}\int_0^L \varphi_i\ \partial_x b_{\Delta x}\ \partial_x h_{\Delta x}\ \varphi_j\ -\ \frac{1}{2}\int_0^L \partial_x\varphi_i\ h_{\Delta x}\ \partial_x b_{\Delta x}\ \varphi_j\ + \\ & - \frac{1}{2}\int_0^L \varphi_i\ h_{\Delta x}\ \partial_x b_{\Delta x}\ \partial_x\varphi_j\ +\ \int_0^L \varphi_i\ (\partial_x b_{\Delta x})^2\ \varphi_j\end{aligned} \tag{12}$$

$$\begin{aligned}\mathrm{Q}_{i,j}(h_{\Delta x}, b_{\Delta x}, \omega_{b\Delta x}) = \ & -\frac{2}{3}\int_0^L \partial_x\varphi_i\ h^3_{\Delta x}\ (\partial_x\varphi_j)^2\ +\ \int_0^L \varphi_i\ \partial_x b_{\Delta x}\ h^2_{\Delta x}\ (\partial_x\varphi_j)^2\ + \\ & + \int_0^L \varphi_i\ \omega_{b\Delta x}\ h^2_{\Delta x}\ \varphi_j\ \partial_x\varphi_j\ +\ \int_0^L \varphi_i\ \omega_{b\Delta x}\ h_{\Delta x}\ \partial_x h_{\Delta x}\ \varphi_j^2\ + \\ & + \frac{1}{2}\int_0^L \varphi_i\ \partial_x\omega_{b\Delta x}\ h^2_{\Delta x}\ \varphi_j^2\ +\ \int_0^L \varphi_i\ \partial_x b_{\Delta x}\ \omega_{b\Delta x}\ h_{\Delta x}\ \varphi_j^2\end{aligned} \tag{13}$$

ω and ω_b are just auxiliary variables that have been introduced such to be able to manage the higher (third) order terms using low order basis functions.

$$\mathrm{M}^{\mathrm{G}}\omega = \int_0^L \varphi_i\ h_{\Delta x}\ \partial_x\eta_{\Delta x} \tag{14}$$

$$\mathrm{M}^{\mathrm{G}}\omega_b = -\int_0^L \partial_x\varphi_i\ \partial_x b_{\Delta x} \tag{15}$$

The linear systems (14) and (15) can be solved very efficiently, being M^{G} symmetric, positive defined and constant. Its LU decomposition can even be stored, reducing the reconstruction of the values of these auxiliary variables to a matrix-vector product. On the contrary, the properties of the matrix $(\mathrm{M}^{\mathrm{G}}+\alpha\mathrm{T})$ cannot be known *a priori*. The solution of the linear algebraic system (8) is thus the most computational demanding process of this phase.

The kind of discretization performed allows many degrees of freedom in the management of the several Galerkin mass matrix M^{G} which appear in it and that can be lumped (or not) always remaining second order accurate. The optimization of the linear dispersion properties of the resulting schemes (see section §5) together with the research of the simplest configuration possible led us to the choice of performing the lumping only in equation (15). This does not affect the linear dispersion properties of the scheme, due to the fact that Q is nonlinear and that b is time-independent; so ω_b can be computed once at the beginning of the calculus and kept all along the simulation.

3.3 Hyperbolic phase : Finite Volume Scheme

Setting $\mathbf{U} = [h,\, hu]^T$, we will use the FV scheme to write the equations for averages of $\mathbf{U}$ over the cells C_i, namely for

$$\mathbf{U}_i(t) = \frac{1}{\Delta x}\int_{C_i} \mathbf{U}(x,t)\,.$$

Using (6)-(7), and following [5, 12, 21, 39], the semi-discrete form of the equations can now be written as :

$$\frac{d}{dt}\mathbf{U}_i = -\frac{1}{\Delta x}\left[\mathbf{F}_{i+1/2} - \mathbf{F}_{i-1/2}\right] + \frac{1}{\Delta x}\Delta\mathbf{S}_{b\,i} + \overline{\mathbf{\Phi}} \tag{16}$$

where $\mathbf{F}_{i\pm1/2}$ and $\Delta\mathbf{S}_{bi}$ are the numerical fluxes at each cell interface and the numerical topography source respectively. The last term is where the link with the elliptic phase is made. In particular, we have

$$\overline{\mathbf{\Phi}} = \frac{1}{\Delta x}\int_{C_i}\begin{pmatrix} 0 \\ \phi_{\Delta x}\end{pmatrix} = \frac{1}{8}\begin{pmatrix} 0 \\ \phi_{i-1}+6\phi_i+\phi_{i+1}\end{pmatrix}$$

having integrated exactly over C_i the piecewise linear polynomial $\phi_{\Delta x}$ obtained from the elliptic phase discussed in the previous section. The numerical fluxes $\mathbf{F}_{i\pm1/2}$ at the cell interfaces can be evaluated by means of an exact or approximate Riemann solver. In this work we used the approximate Riemann solver of Roe [45] along with an upwind discretization of the topography source. The source terms are numerical treated as to satisfy the C-property and can be easily incorporated in this solver. The numerical fluxes in (16) are defined as:

$$\mathbf{F}_{i+1/2} = \mathbf{F}_{i+1/2}(\mathbf{U}^L_{i+1/2}, \mathbf{U}^R_{i+1/2}) = \frac{1}{2}\left(\mathbf{F}(\mathbf{U}^R_{i+1/2}) + \mathbf{F}(\mathbf{U}^L_{i+1/2})\right) - \frac{1}{2}|\mathbf{A}|_{i+1/2}\Delta_{i+1/2}\mathbf{U} \tag{17}$$

where $\Delta(\cdot)_{i+1/2} = (\cdot)^R_{i+1/2} - (\cdot)^L_{i+1/2}$. $\mathbf{A}_{i+1/2}$ is the Roe average Jacobian matrix and is equal to $\left[\mathbf{X}|\mathbf{\Lambda}|\mathbf{X^{-1}}\right]_{i+1/2}$, where $\mathbf{X}_{i+1/2}$ and $\mathbf{X}^{-1}_{i+1/2}$ are the left and right eigenvector matrices respectively and $\mathbf{\Lambda}$ is the diagonal matrix with the eigenvalues in the diagonal.

The numerical integration with the upwind scheme presented up to now lead to approximations that are only first order accurate, if a constant distribution is assumed in each computational cell C_i. To achieve higher accuracy we evaluate the left and right states using a third order MUSCL extrapolation scheme [59, 26]. The reconstruction is performed for the variables $[h,\, u]$ as well as for the topography b. For the $(i+1/2)$ interface the reconstructed values of the total water depth can be written as

$$\begin{aligned} h^L_{i+1/2} =& h_i + \frac{\psi(r_i)}{4}\left[(1-\kappa)\Delta h_{i-1/2} + (1+\kappa)\Delta h_{i+1/2}\right] \\ h^R_{i+1/2} =& h_{i+1} - \frac{\psi(r_{i+1})}{4}\left[(1-\kappa)\Delta h_{i+3/2} + (1+\kappa)\Delta h_{i+1/2}\right] \end{aligned} \tag{18}$$

where ψ is the limiter function with $r_i = \frac{\Delta h_{i-1/2}}{\Delta h_{i+1/2}}$, and where third order of accuracy in smooth regions is obtained for $\kappa = 1/3$. In this work the widely known min-mode and MC limiters are used [29].

To guarantee the exact preservation of steady state still flat free surface states, the so-called C-property [5], an upwind discretization scheme is also used for the bed topography source terms $\mathbf{S}_b$. In particular, following [5, 21], the source term in (16) contains the following two terms

$$\Delta \mathbf{S}_{b,\,i} = \mathbf{S}^-_{b,\,i+1/2}(\mathbf{U}^L_{i+1/2}, \mathbf{U}^R_{i+1/2}) + \mathbf{S}^+_{b,\,i-1/2}(\mathbf{U}^L_{i-1/2}, \mathbf{U}^R_{i-1/2}) \tag{19}$$

where

$$\begin{aligned} \mathbf{S}^+_{b\,i+1/2}(\mathbf{U}^L_{i+1/2}, \mathbf{U}^R_{i+1/2}) =& \frac{1}{2}\left[\mathbf{X}(\mathbf{I} + \mathbf{\Lambda}^{-1}|\mathbf{\Lambda}|)\mathbf{X}^{-1}\right]_{i+1/2} \widetilde{\mathbf{S}}_{b\,i+1/2}(\mathbf{U}^L_{i+1/2}, \mathbf{U}^R_{i+1/2}) \\ \mathbf{S}^-_{b\,i+1/2}(\mathbf{U}^L_{i+1/2}, \mathbf{U}^R_{i+1/2}) =& \frac{1}{2}\left[\mathbf{X}(\mathbf{I} - \mathbf{\Lambda}^{-1}|\mathbf{\Lambda}|)\mathbf{X}^{-1}\right]_{i+1/2} \widetilde{\mathbf{S}}_{b\,i+1/2}(\mathbf{U}^L_{i+1/2}, \mathbf{U}^R_{i+1/2}) \end{aligned} \tag{20}$$

and with

$$\widetilde{\mathbf{S}}_{b\,i+1/2}(\mathbf{U}^L_{i+1/2}, \mathbf{U}^R_{i+1/2}) = \left[\begin{array}{c} 0 \\ -g\dfrac{h^L + h^R}{2}\left(b^R - b^L\right) \end{array}\right]_{i+1/2}. \tag{21}$$

Using the above and for the first order scheme, the numerical flux term discretization balances with the topography source term discretization for hydrostatic conditions, which gives in each mesh cell $u = 0$ and $b^R - b^L = -\left(h^R - h^L\right)$. While this holds for the first order scheme, this is not the case when using higher reconstructions as we do here. In this case, following [21, 39] we include the additional correction term $\mathbf{S}^\star_b$ for maintaining the correct balance i.e.

$$\Delta \mathbf{S}_{b\,i} = \mathbf{S}^-_{b\,i+1/2} + \mathbf{S}^+_{b\,i-1/2} + \mathbf{S}^\star_b\left(\mathbf{U}^L_{i+1/2}, \mathbf{U}^R_{i-1/2}\right). \tag{22}$$

with

$$\mathbf{S}^\star_b\left(\mathbf{U}^L_{i+1/2}, \mathbf{U}^R_{i-1/2}\right) = \left[\begin{array}{c} 0 \\ -g\dfrac{h^R_{i-1/2} + h^L_{i+1/2}}{2}\left(b^R_{i-1/2} - b^L_{i+1/2}\right) \end{array}\right].$$

3.4 Hyperbolic phase : Finite Element Scheme

Two FE methods are considered here. The first is a classical C^0 Galerkin approximation of the two equations (7). For an internal node i the discrete continuous Galerkin equations are readily obtained by evaluating the integrals (set $q = hu$)

$$\begin{aligned} \int_0^L \varphi_i \partial_t h_{\Delta x} - \int_0^L \partial_x \varphi_i q_{\Delta x} = 0 \\ \int_0^L \varphi_i \partial_t q_{\Delta x} - \int_0^L \partial_x \varphi_i \left[\frac{q_{\Delta x}^2}{h_{\Delta x}} + g \frac{h_{\Delta x}^2}{2} \right] - \int_0^L \varphi_i \tilde{S}_b = \int_0^L \varphi_i \phi_{\Delta x} \end{aligned} \tag{23}$$

with $\tilde{S}_b = -gh\partial_x b$. With the notation of the previous section, the integrals can be approximated as [44]

$$\mathbf{M}^{\mathrm{G}} \frac{d}{dt}\mathbf{U} = -\frac{1}{2}\left[\mathbf{F}(\mathbf{U}_{i+1}) - \mathbf{F}(\mathbf{U}_{i-1})\right] + \frac{1}{2}\tilde{\mathbf{S}}_{b\,i+1/2} + \frac{1}{2}\tilde{\mathbf{S}}_{b\,i-1/2} + \overline{\mathbf{\Phi}}^{\mathrm{G}} \tag{24}$$

where $\mathbf{M}^{\mathrm{G}}$ is the Galerkin mass matrix defined in (11).
By analogy with (16), we use the notation $\overline{\mathbf{\Phi}}$ for the contribution of the non-hydrostatic terms, which in this case is given by

$$\overline{\mathbf{\Phi}}^{\mathrm{G}} = \mathbf{M}^{\mathrm{G}} \mathbf{\Phi}\,. \tag{25}$$

As shown in [58, 44], scheme (24) is fourth order accurate in space when the shallow water limit is considered.

To obtain a discretization with some shock capturing capabilities, we consider the upwind stabilized method used in [44, 2, 3] (see also [22]). In particular, introducing the local residual

$$\mathbf{R}_{\Delta x} = \begin{pmatrix} \partial_t h_{\Delta x} + \partial_x q_{\Delta x} \\ \partial_t q_{\Delta x} + \partial_x (q_{\Delta x}^2/h_{\Delta x} + g h_{\Delta x}^2/2) - \tilde{S}_b - \phi_{\Delta x} \end{pmatrix}, \tag{26}$$

obtained by replacing in the continuous equations the discrete approximation of the unknowns, we consider the streamline upwind scheme :

$$\mathbf{M}^{\mathrm{G}} \frac{d}{dt}\mathbf{U} = -\frac{1}{2}\left[\mathbf{F}(\mathbf{U}_{i+1}) - \mathbf{F}(\mathbf{U}_{i-1})\right] + \frac{1}{2}\tilde{\mathbf{S}}_{b\,i+1/2} + \frac{1}{2}\tilde{\mathbf{S}}_{b\,i-1/2} + \overline{\mathbf{\Phi}}^{\mathrm{G}} - \sum_{j=0}^{1} \int_{x_{i+j-1}}^{x_{i+j}} A \partial_x \varphi_i \, \tau_{\mathrm{SU}} \, \mathbf{R}_{\Delta x}\,.$$

In the last expression, the matrix τ_{SU} is a scaling parameter in practice defined as [22, 44]

$$\tau_{\mathrm{SU}} = \frac{\Delta x}{2} |A|^{-1}\,.$$

With this definition, using (26) and the notation of section §3.2, one easily shows that the streamline upwind scheme can be written as

$$\mathbf{M}^{\mathrm{SU}} \frac{d}{dt}\mathbf{U} = -\left[\mathbf{F}_{i+1/2}(\mathbf{U}_i, \mathbf{U}_{i+1}) - \mathbf{F}_{i+1/2}(\mathbf{U}_{i-1}, \mathbf{U}_i)\right] + \mathbf{S}^-_{b\,i+1/2}(\mathbf{U}_i, \mathbf{U}_{i+1}) + \mathbf{S}^+_{b\,i-1/2}(\mathbf{U}_{i-1}, \mathbf{U}_i)\, \overline{\mathbf{\Phi}}^{\mathrm{SU}} \tag{27}$$

where the numerical fluxes and sources have exactly the same expression as in (17) and (20), respectively, and where the entries of the Streamline Upwind mass matrix now couple the h and q ODEs and depend on the sign of the shallow water flux Jacobian matrix A. In particular

$$\left[\mathbf{M}^{\text{SU}}\mathbf{V}\right]_i = \frac{\Delta x}{6}\mathbf{V}_{i-1}+\frac{2\Delta x}{3}\mathbf{V}_i+\frac{\Delta x}{6}\mathbf{V}_{i+1}+\frac{\Delta x}{4}\text{sign}(A_{i-1/2})\Big(\mathbf{V}_{i-1}+\mathbf{V}_i\Big)-\frac{\Delta x}{4}\text{sign}(A_{i+1/2})\Big(\mathbf{V}_{i+1}+\mathbf{V}_i\Big) \tag{28}$$

By analogy with (16), we have used the notation $\overline{\mathbf{\Phi}}$ for the contribution of the non-hydrostatic terms, which in this case is given by

$$\overline{\mathbf{\Phi}}^{\text{SU}} = \mathbf{M}^{\text{SU}}\mathbf{\Phi}\,.$$

As shown in [44, 2, 3], to which we refer for all additional details, the stabilized FE method (27) is third order accurate in space when the shallow water limit is considered, and it preserves exactly steady state still flat free surface states.

Finally, in order to handle moving bores and dry areas, we introduce as in [2, 3] the following nonlinear splitting of the mass matrix (sc stands for shock capturing) :

$$\begin{aligned}\left[\mathbf{M}^{\text{SU-sc}}\mathbf{V}\right]_i = \Delta x\mathbf{V}_i+\psi_{i+1/2}\frac{\Delta x}{2}\left[\frac{1}{3}\Big(\mathbf{V}_{i+1}-\mathbf{V}_i\Big)-\frac{\text{sign}(A_{i+1/2})}{2}\Big(\mathbf{V}_{i+1}+\mathbf{V}_i\Big)\right]\\ +\psi_{i-1/2}\frac{\Delta x}{2}\left[\frac{1}{3}\Big(\mathbf{V}_{i-1}-\mathbf{V}_i\Big)+\frac{\text{sign}(A_{i-1/2})}{2}\Big(\mathbf{V}_{i-1}+\mathbf{V}_i\Big)\right]\end{aligned} \tag{29}$$

The final form of the scheme reads

$$\mathbf{M}^{\text{SU-sc}}\frac{d}{dt}\mathbf{U} = -\left[\mathbf{F}_{i+1/2}(\mathbf{U}_i,\mathbf{U}_{i+1})-\mathbf{F}_{i+1/2}(\mathbf{U}_{i-1},\mathbf{U}_i)\right]+\mathbf{S}^-_{b\,i+1/2}(\mathbf{U}_i,\mathbf{U}_{i+1})+\mathbf{S}^+_{b\,i-1/2}(\mathbf{U}_{i-1},\mathbf{U}_i)\Delta x \tag{30}$$

The quantity $\psi_{i\pm1/2}$ in (29) is a limiter function. For $\psi = 0$ the scheme reduces to the first order version of Roe's scheme, which is basically the first order version of (16). For $\psi = 1$ the third order finite element method (27) is recovered. Any function can be used to detect smooth areas and dry or shocked regions.

Here, we use the smoothness sensor proposed in [2, 3] and based on two different approximation of the curvature of the free surface elevation η :

$$\psi_{i+1/2} = \min(\psi_i,\psi_{i+1})\,,\qquad \psi_i = \min\left(1,\,\alpha\frac{|\int_0^L\varphi_i\partial_x\eta_{\Delta x}|}{|\int_0^L\partial_x\varphi_i\partial_x\eta_{\Delta x}+V_i|}\right)$$

where V_i is obtained as the fourth order finite difference approximation of $\partial_{xx}\eta_i$, and with $\alpha = \frac{1}{9}$ as in [2, 3].

3.5 Well-balancing, wet/dry front treatment, mass conservation

In order to identify the dry cells we use the technique described in [43, 42]. In particular, we introduce two threshold parameters ϵ_h^{wd} and ϵ_u^{wd} acting independently on the water height and the velocity respectively. So if H in a node

is less that ϵ_h^{wd}, that node is considered as dry. This parameter is very small, compared to the mesh size. Typical values range between $10^{-9} - 10^{-6}$. The second parameter is used to avoid division by zero and is set to

$$\epsilon_u^{wd} = \frac{\Delta x^2}{L^2}$$

with L the length of the spatial domain. If in a node $h \leq \epsilon_u^{wd}$, the velocity in that node is set to zero. To avoid loosing mass, and guarantee absolute mass conservation we follow the treatments proposed in [18, 11, 31] where the total mass in nodes with $h \leq \epsilon_u^{wd}$ is redistributed uniformly to the rest of the domain.

Furthermore, the presence of dry areas should not affect the ability of the schemes to preserve steady states involving flat free surface still water. To ensure this property, we use a standard technique consisting in redefining the bed elevation at the emerging dry cell [12, 11] as:

$$\Delta b = \begin{cases} h^L & \text{if } h^L > \epsilon_h^{wd} \text{ and } h^R \leq \epsilon_h^{wd} \text{ and } b^R < (b^R - b^L) \\ (b^L - b^R) & \text{otherwise} \end{cases} \tag{31}$$

when a wet/dry front exists between computational cells with (reconstructed) face values L and R. For both FV and FE schemes this modification is applied in the computation of the source term $\tilde{\mathbf{S}}_b$. A similar treatment holds if R is wet and L dry. Just for the FV scheme and for the flow in motion over adverse slopes, further modifications are made following [13, 24]. Finally, and as to properly detect regions in proximity of dry areas, we use an exponential filter proposed in [43, 42]. This exponential function is embedded in the limiters and activated whenever the limiter is on.

4 Time integration, boundary conditions, and friction

4.1 High order time integration methods

Similarly to the spatial domain, the temporal domain is discretized by a set of non-overlapping slabs $[t^n, t^{n+1}]$. We will denote by $\Delta t^{n+1} = t^{n+1} - t^n$. For generality, three different time discretizations are compared in this work. One is a method quite classical in the context of Boussinesq type numerical models, while the other two have been chosen as representatives of boundedness or strong stability preserving methods. For all of these methods, the time step is computed by means of the standard condition

$$\Delta t^{n+1} = \mathrm{CFL} \frac{\Delta x}{\max_i(|u_i^n| + \sqrt{g h_i^n})}$$

For the shallow water equations, the stability condition for the first order methods used here is $\mathrm{CFL}_c = 1$ when using the first order explicit Euler method. For the high order methods used below we will speak of efficiency as the ratio CFL_c/p, with p the number of right hand side evaluations in one time step.

The first time integration scheme we consider is the fourth order in time Adams Bashforth-Adams Moulton (AM4) method well known in the community

of Boussinesq modelling [60, 46]. For the ODE

$$\mathbf{U}' = \mathcal{L}(\mathbf{U})$$

this time integration scheme requires in two stages :

1. Predictor stage (Adams-Basforth method)

$$\mathbf{U}^p = \mathbf{U}^n + \frac{\Delta t}{12}\left[23\mathcal{L}(\mathbf{U}^n) - 16\mathcal{L}(\mathbf{U}^{n-1}) + 5\mathcal{L}(\mathbf{U}^{n-2})\right] \tag{32}$$

2. Corrector stage (Adams-Moulton method)

$$\mathbf{U}^{n+1} = \mathbf{U}^n + \frac{\Delta t}{24}\left[9\mathcal{L}(\mathbf{U}^p) + 19\mathcal{L}(\mathbf{U}^n) - 5\mathcal{L}(\mathbf{U}^{n-1}) + \mathcal{L}(\mathbf{U}^{n-2})\right] \tag{33}$$

The Adams predictor corrector has stability properties close to those of the explicit Euler scheme, with respect to which we thus have an efficiency of $1/2$ (2 stages for the same time step magnitude).

We also test the three stages third order SSP Runge-Kutta (RK3) scheme reading [19]

1. First predictor

$$\mathbf{U}^p = \mathbf{U}^n + \Delta t\, \mathcal{L}(\mathbf{U}^n) \tag{34}$$

2. Second predictor

$$\mathbf{U}^{2p} = \frac{3}{4}\mathbf{U}^n + \frac{1}{4}\mathbf{U}^n + \frac{\Delta t}{4}\mathcal{L}(\mathbf{U}^p) \tag{35}$$

3. Final stage :

$$\mathbf{U}^{n+1} = \frac{1}{3}\mathbf{U}^n + \frac{2}{3}\mathbf{U}^{2p} + \frac{2\Delta t}{3}\mathcal{L}(\mathbf{U}^{2p}) \tag{36}$$

The RK3 belongs to the family of strong stability preserving multi-stage methods with positive coefficients, inheriting the same stability properties of the explicit Euler scheme. In particular, compared to the latter, the RK3 has a CFL condition of 1 (cf. [19] for details), giving an efficiency of $1/3$.

Lastly, we have tested the third order explicit backward differencing method (eBDF3) [27] reading

$$\alpha_{n+1}\mathbf{U}^{n+1}+\alpha_n\mathbf{U}^n+\alpha_{n-1}\mathbf{U}^{n-1}+\alpha_{n-2}\mathbf{U}^{n-2} = \beta_n\,\mathcal{L}(\mathbf{U}^n)+\beta_{n-1}\,\mathcal{L}(\mathbf{U}^{n-1})+\beta_{n-2}\,\mathcal{L}(\mathbf{U}^{n-2}) \tag{37}$$

where the weights take the form

$$\alpha_{n+1} = \frac{1}{\Delta t^{n+1}} + \frac{1}{\Delta t^{n+1}+\Delta t^n} + \frac{1}{\Delta t^{n+1}+\Delta t^n+\Delta t^{n-1}}\,, \quad \alpha_n = -\frac{(\Delta t^{n+1}+\Delta t^n)(\Delta t^{n+1}+\Delta t^n+\Delta t}{\Delta t^{n+1}\Delta t^n(\Delta t^n+\Delta t^{n-1})}$$

$$\alpha_{n-1} = \frac{\Delta t^{n+1}(\Delta t^{n+1}+\Delta t^n+\Delta t^{n-1})}{(\Delta t^{n+1}+\Delta t^n)\Delta t^n\Delta t^{n-1}}\,, \quad \alpha_{n-2} = -\frac{\Delta t^{n+1}(\Delta t^{n+1}+\Delta t^n}{(\Delta t^{n+1}+\Delta t^n+\Delta t^{n-1})(\Delta t^n+}$$

and

$$\beta_n = \frac{(\Delta t^{n+1} + \Delta t^n)(\Delta t^{n+1} + \Delta t^n + \Delta t^{n-1})}{\Delta t^n (\Delta t^n + \Delta t^{n-1})}\,,\quad \beta_{n-1} = -\frac{\Delta t^{n+1}(\Delta t^{n+1} + \Delta t^n + \Delta t^{n-1})}{\Delta t^n \Delta t^{n-1}}\,,\quad \beta_{n-2} = \frac{\Delta t^{n+1}(\Delta t^{n+1} +$$

The eBDf3 is part of a family of high order explicit multi step methods verifying, under a time step restriction, the same boundedness preserving property of the explicit Euler scheme. Compared to the latter, the eBDf3 has a CFL condition of $1/3$ (cf. [23] for details), which gives the same efficiency of the RK3 method.

4.2 Boundary conditions and the internal source function

To define the differential problems boundary conditions must be introduced. In this work we use two types of boundary conditions depending on the examined test case: solid (reflective) wall and absorbing boundary conditions. For the FV scheme, in a computational domain the reconstructed values, for the third-order MUSCL scheme, on the first and last cell are computed using neighboring ghost cells. More informations can be found at [24] . For the FE scheme ghost cells are in no need since it is a node centered scheme and the degrees of freedom are located directly on the physical boundary.

Absorbing boundaries are also applied and dissipate the energy of incoming waves perfectly in order to eliminate non physical reflections. In front of this kind of boundaries a sponge layer is defined. On this layer the surface elevation and the momentum are damped by multiplying their values by a coefficient $m(x)$ defined as [25]

$$m(x) = \sqrt{1 - \left(\frac{x - d(x)}{L_s}\right)^2}. \tag{38}$$

L_s is the sponge layer width and $d(x)$ is the normal distance between the cell center with coordinates x and the absorbing boundary.The sponge layer width should be $L \leq L_s \leq 1.5L$, i.e. the width of the sponge layer is proportional to the wavelength. Thus, longer wavelengths require longer sponge layers.

Wave generation in the model is achieved by using the internal wave generator of Wei et al. [62]. In [62] the wave generator, of free surface waves, is introduced as a source function added to the mass equation. It is derived using the equations of Nwogu [40] but it can be used for many types of Boussinesq-type equations by changing the dispersion relation used in the generator. In this work, and as to be compatible with the equations of GN, we use the dispersion relation (42).

4.3 Friction terms discretization

An explicit treatment of the friction can produce numerical oscillations [11, 38, 37] when the roughness coefficient is high. For this reason we use the technique proposed by [11, 37]. More precisely, for both schemes at the end of each time step we have :

$$(hu)_i^{n+1} = (hu)_i^\star - g(hS_f)_i^{n+1}\Delta t^n \tag{39}$$

where all the values signed with $\star$ are the values computed without the friction. Using $(S_f)_i = (uR_f)_i = u_i \dfrac{N_m^2 ||u_i||}{h_i^{4/3}}$, and substituting in the above equation we

have :

$$(hu)_i^{n+1} = (hu)_i^\star - g(huR_f)_i^{n+1}\Delta t^n = (hu)_i^\star - g(hu)_i^{n+1}\left[(1-\theta)(R_f)_i^{n+1} + \theta(R_f)_i^n\right]\Delta t^n \tag{40}$$

with N_m being the Manning roughness coefficient. Now, by separating explicit and implicit part and by assuming that $R_f^{n+1} = R_f^\star$ we can write:

$$(hu)_i^{n+1} = \frac{(hu)_i^\star - \theta g(hu)_i^n (R_f)_i^n \Delta t^n}{1 + (1-\theta)g(R_f)_i^\star \Delta t^n} \tag{41}$$

When the implicitness parameter θ is set to zero, the friction source term is computed in a completely implicit manner, while when $\theta = 1$ it is computed in a totally explicit point wise manner. In all the computations shown in this work we have used $\theta = 0$.

5 Semi-discrete dispersion error analyses

5.1 Spatial discretization : time continuous analysis

The analytical expression of the linear dispersion relation for the present model has been already given in section §2 and will be here rewritten:

$$\omega_{\mathrm{GN}}^2 = gh_0k^2\frac{1 + \frac{\alpha-1}{3}k^2h_0^2}{1 + \frac{\alpha}{3}k^2h_0^2}. \tag{42}$$

As already explained, this relation can be recovered by means of a Fourier analysis on a horizontal bottom performed on the linearized system of equations:

$$(I + \alpha T_{LIN})\phi = T_{LIN}(gh_0\eta_x) \tag{43}$$

$$\begin{aligned} \eta_t + h_0u_x &= 0 \\ h_0u_t + gh_0\eta_x &= \phi \end{aligned} \tag{44}$$

where h_0 represents the constant water depth and $T_{LIN}(\cdot) = -\frac{1}{3}h_0^2(\cdot)_{xx}$.

Having a low dispersion error w.r.t. the model, is of paramount importance for any numerical scheme that wants to be applied to the study of near-shore wave propagation. In this section we will perform an analysis on the discrete dispersion relations of the several schemes here implemented: continuous finite element (with and without the upwind stabilization) and finite volume; comparing them and finding the best possible configuration of the discretization which minimize the dispersion error.

We performed our analysis replacing the nodal values of η and u in each discretized scheme by a propagating Fourier mode $W_i = W_0e^{\nu_h t + jkx_i}$; where $\nu_h = \xi_h + j\omega_h$ and ξ_h and ω_h represents respectively the amplification rate and the phase speed. Again k here, represents the wave number of the Fourier mode. The algebraic expression obtained in such a way can be easily rewritten in terms of the nodal value W_i using relations of the type $W_{i\pm1} = e^{\pm jk\Delta x}$. The resulting system of equations constitutes a complex eigenvalue problem, whose solution is the dispersion factor ν_h.

The dispersion formula obtained are hard to interpret, so we chose to present the results in the form of comparison plots, comparing the dispersion error

curves of all the models and w.r.t. the ones corresponding to second order finite different discretization scheme (FD2) and fourth order finite difference discretization scheme (FD4). For the sake of brevity and clarity, in the following we will just present the concluding remarks. Please refer to the appendix for more details.

5.1.1 Finite element

Discretizing the system (43) - (44) using the centered Galerkin FE scheme described by (24) and applying the procedure described above, the following set of equations will be found:

$$\left(\tilde{\mathrm{M}}^{\mathrm{G}} - \frac{\alpha h_0^2}{3}\tilde{\mathrm{S}}^{\mathrm{G}}\right)\phi_i = -\frac{g h_0^3}{3}\tilde{\mathrm{T}}^{\mathrm{G}}\left(\tilde{\mathrm{M}}^{\mathrm{G}}\right)^{-1}\eta_i \tag{45}$$

$$\begin{aligned} \tilde{\mathrm{M}}^{\mathrm{G}}\nu_h\eta_i + h_0\tilde{\mathrm{F}}^{\mathrm{G}}u_i &= 0 \qquad (46)\\ \tilde{\mathrm{M}}^{\mathrm{G}}\nu_h u_i + g\tilde{\mathrm{F}}^{\mathrm{G}}\eta_i &= \frac{1}{h_0}\tilde{\mathrm{M}}^{\mathrm{G}}\phi_i \end{aligned}$$

The writing of the Jacobian matrix of the system (46) and of its characteristic polynomial lead to a complex algebraic equation, whose solution in the real part allows to obtain the final discrete dispersion relation of the Galerkin scheme:

$$\left(\omega_h^{\mathrm{G}}\right)^2 = \frac{g h_0\left(\tilde{\mathrm{F}}^{\mathrm{G}}\right)^2 - \tilde{\mathrm{F}}^{\mathrm{G}}\tilde{\mathrm{M}}^{\mathrm{G}}\tilde{\Phi}_{LIN}}{\left(\tilde{\mathrm{M}}^{\mathrm{G}}\right)^2} \tag{47}$$

Please refer to the Appendix for the definitions of the quantities: $\tilde{\mathrm{M}}^{\mathrm{G}}$, $\tilde{\mathrm{F}}^{\mathrm{G}}$, $\tilde{\mathrm{S}}^{\mathrm{G}}$, $\tilde{\mathrm{T}}^{\mathrm{G}}$ and $\tilde{\Phi}_{LIN}$.

Figure 2 shows the relative dispersion error $\mid \omega_h^{\mathrm{G}} - \omega_{\mathrm{GN}} \mid / \omega_{\mathrm{GN}}$ of the Galerkin scheme w.r.t. equation (42), obtained for the two values $kh_0 = 0.5$ and $kh_0 = 2.5$. In the pictures the relative errors of the FD2 and FD4 discretization schemes are also reported as a reference. On the x-axis we have the inverse of the number of nodes per wavelength. The mathematical expressions of ω_h^{FD2} and ω_h^{FD4} are also given in the appendix. We can see that the centered Galerkin scheme provides a dispersion error which is comparable, and for $kh_0 = 0.5$ even better, to those of the FD4 scheme.

In section §3.2 we mentioned the degrees of freedom which comes out when the elliptic problem (6) is discretized by means of the continuous finite element approach. The possibility to choose to lump or not the several mass matrices of equations (8), (14) and (15) influences the form of equation (45). As a consequence, the $\tilde{\Phi}_{LIN}$ tensor assumes different forms (see the appendix for more details) and the dispersion relation of the scheme is deeply affected by these devices according to what rapresented in figure 3. We have already mentioned that the choice of lumping the mass matrix in (15) does not affect the linear dispersion relation, since it belongs to the nonlinear term R. Thus the best possible configuration, which minimize the dispersion error of the scheme, must be searched among only four different options. We invite the readers interested to the description of the several configurations to the appendix; here we just limit ourself to named them from 1 to 4 and sketch their dispersion error curves

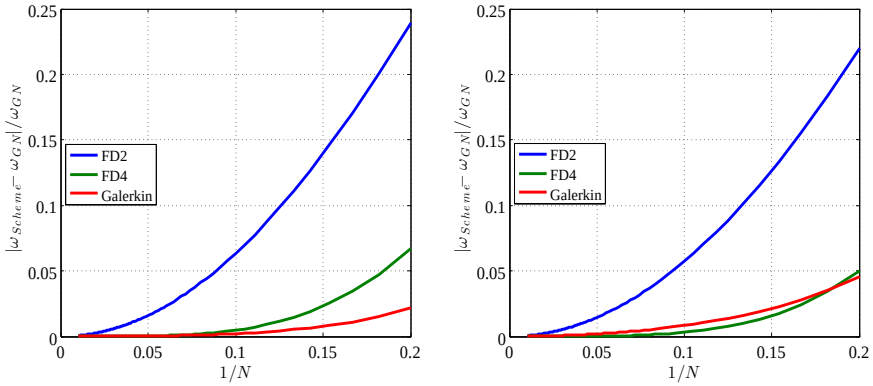

Figure 2: Dispersion error for the centered Galerkin FE scheme for $kh_0 = 0.5$ (left) and $kh_0 = 2.5$ (right): comparison w.r.t. the FD2 and FD4 schemes.

in the figure 3. We can see that the several configurations provide similar results for $kh_0 = 0.5$, even better w.r.t the FD4 one; while for $kh_0 = 2.5$ (deeper waters) they diverge significantly and only the variants 3 and 4 remain close to the fourth order scheme accuracy.

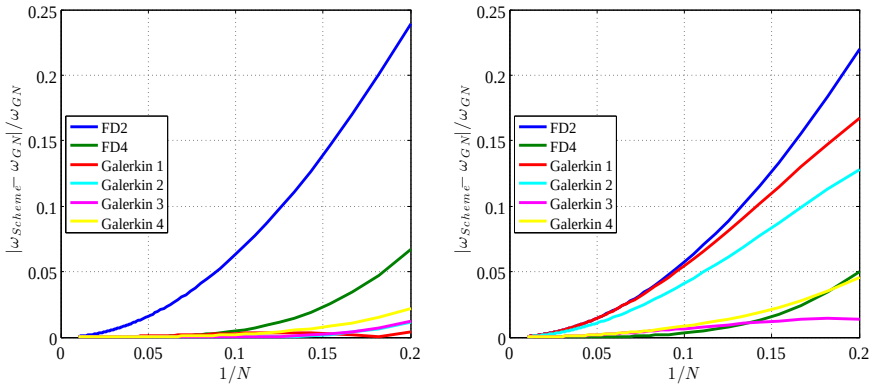

Figure 3: Dispersion error for the centered Galerkin FE scheme for $kh_0 = 0.5$ (left) and $kh_0 = 2.5$ (right): comparison among the different configurations possible for the elliptic phase solution.

The same analysis can be performed for the upwind stabilized finite element scheme (SUPG). Being $c = gh_0$ the celerity of the wave, the sign of the Jacobian matrix of the linear shallow water fluxes, which pre-multiplies the upwind terms in (28), has the form:

$$\text{sign}(A) = \begin{bmatrix} 0 & c/g \\ g/c & 0 \end{bmatrix}.$$

Discretizing system (43) by means of the SUPG scheme will now lead to:

$$\left(\tilde{\mathrm{M}}^{\mathrm{G}} - \frac{\alpha h_0^2}{3}\tilde{\mathrm{S}}^{\mathrm{G}}\right)\phi_i = -\frac{g h_0^3}{3}\tilde{\mathrm{T}}^{\mathrm{G}}\left(\tilde{\mathrm{M}}^{\mathrm{G}}\right)^{-1}\eta_i \tag{48}$$

$$\begin{aligned}
\tilde{\mathrm{M}}^{\mathrm{G}}\nu_h\eta_i + h_0\tilde{\mathrm{F}}^{\mathrm{G}}u_i - \frac{c}{2g}\left[\tilde{\mathrm{M}}^{\mathrm{UFE}}\nu_h u_i + g\tilde{\mathrm{F}}^{\mathrm{UFE}}\eta_i - \frac{1}{h_0}\tilde{\mathrm{M}}^{\mathrm{UFE}}\phi_i\right] &= 0 \\
\tilde{\mathrm{M}}^{\mathrm{G}}\nu_h u_i + g\tilde{\mathrm{F}}^{\mathrm{G}}\eta_i - \frac{g}{2c}\left[\tilde{\mathrm{M}}^{\mathrm{UFE}}\nu_h\eta_i + h_0\tilde{\mathrm{F}}^{\mathrm{UFE}}u_i\right] &= \frac{1}{h_0}\tilde{\mathrm{M}}^{\mathrm{G}}\phi_i
\end{aligned} \tag{49}$$

Please refer to the appendix for the definitions of $\tilde{\mathrm{M}}^{\mathrm{UPE}}$ and $\tilde{\mathrm{F}}^{\mathrm{UPE}}$. Note that equation (48) remains equal to (45) since the stabilization procedure only affects the hyperbolic part of the problem.

As before, the writing of the Jacobian matrix of the system (49) and of its characteristic polynomial lead to a complex algebraic equation, whose solution in the real part is:

$$\left(\omega_h^{\mathrm{SU}}\right)^2 = \frac{\mathrm{A}_S^{\mathrm{SU}}}{\mathrm{A}_{\nu^2}^{\mathrm{SU}}} - \left(\frac{\mathrm{A}_\nu^{\mathrm{SU}}}{2\mathrm{A}_{\nu^2}^{\mathrm{SU}}}\right)^2 \tag{50}$$

being $\mathrm{A}_{\nu^2}^{\mathrm{SU}}$, $\mathrm{A}_\nu^{\mathrm{SU}}$ and $\mathrm{A}_S^{\mathrm{SU}}$ functions of the quantities $\tilde{\mathrm{M}}^{\mathrm{G}}$, $\tilde{\mathrm{F}}^{\mathrm{G}}$, $\tilde{\mathrm{M}}^{\mathrm{UPE}}$, $\tilde{\mathrm{F}}^{\mathrm{UPE}}$ and $\tilde{\Phi}_{LIN}$, whose expressions are written in details in the appendix. Figure 4 shows the comparison of the dispersion error of the SUPG scheme for the two values $kh_0 = 0.5$ and $kh_0 = 2.5$ w.r.t. the errors provided by the FD2, FD4 and Galerkin schemes. We can see that the dispersion error of the stabilized scheme behaves better w.r.t. the centered scheme one, given better accuracy even for $kh_0 = 2.5$ and confirming the results already mentioned in [44] about the application of such methods on the discretization of the Madsen and Sørensen model [34].

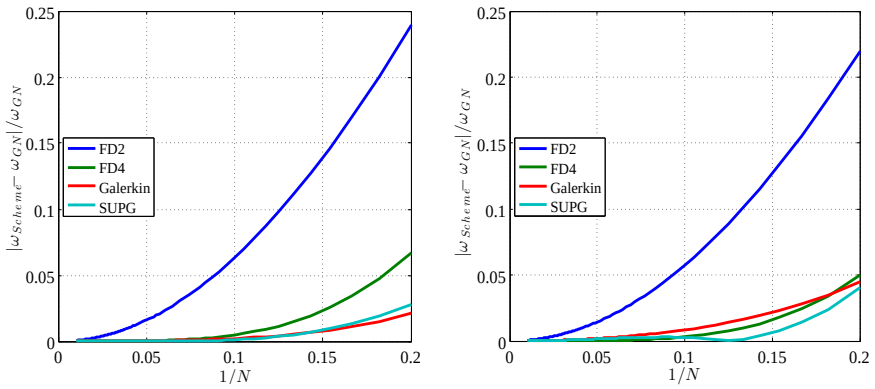

Figure 4: Dispersion error for the stabilized upwind FE (SUPG) scheme for $kh_0 = 0.5$ (left) and $kh_0 = 2.5$ (right): comparison w.r.t. the FD2, FD4 and centered Galerkin schemes.

The several possible configurations of equation (48) affect the form of the dispersion relation also in this case. Figure 5 compares the dispersion error curves provided by the several cases. The results confirm what already observed

for the Galrkin scheme. In fact, all the configurations provide similar results for $kh_0 = 0.5$, while only the configurations 3 and 4 perform accurate results when $kh_0 = 2.5$. In this case only the case 4, which correspond not to lump any mass matrices of the equations (8) and (14), performs always better than the fourth order scheme in deep waters. For this reason it has been implemented and used to perform the simulations presented in the next sections of the paper.

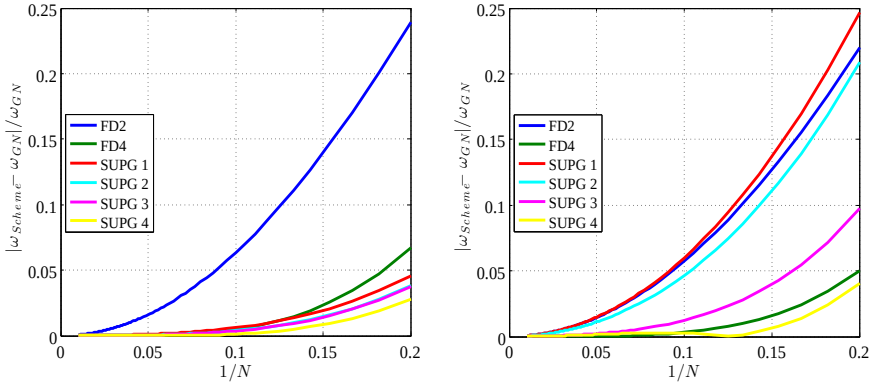

Figure 5: Dispersion error for the stabilized upwind FE (SUPG) scheme for $kh_0 = 0.5$ (left) and the $kh_0 = 2.5$ (right): comparison among the different configurations possible for the elliptic phase solution.

5.1.2 Finite volume

Last but not least, we perform the same study for the FV scheme. Using the linearized equations (44) and the FV scheme with the third order MUSCL reconstruction, described in section §3.3, we get for the following system:

$$\left(\tilde{\mathrm{M}}^{\mathrm{G}} - \frac{\alpha h_0^2}{3}\tilde{\mathrm{S}}^{\mathrm{G}}\right)\phi_i = -\frac{g h_0^3}{3}\tilde{\mathrm{T}}^{\mathrm{G}}\left(\tilde{\mathrm{M}}^{\mathrm{G}}\right)^{-1}\eta_i \tag{51}$$

$$\nu_h \eta_i + h_0 \tilde{\mathrm{F}}^{\mathrm{FV}} u_i - c\tilde{\mathrm{F}}^{\mathrm{UFV}}\eta_i = 0 \tag{52}$$

$$\nu_h u_i + g\tilde{\mathrm{F}}^{\mathrm{FV}}\eta_i - c\tilde{\mathrm{F}}^{\mathrm{UFV}} u_i = \frac{1}{h_0}\tilde{\mathrm{M}}^{\mathrm{FV}}\phi_i$$

which, by means of the procedure already described above, lead to the final form of the dispersion relation:

$$\left(\omega_h^{\mathrm{SU}}\right)^2 = \frac{\mathrm{A}_S^{\mathrm{FV}}}{\mathrm{A}_{\nu^2}^{\mathrm{FV}}} - \left(\frac{\mathrm{A}_\nu^{\mathrm{FV}}}{2\mathrm{A}_{\nu^2}^{\mathrm{FV}}}\right)^2 \tag{53}$$

being $\mathrm{A}_{\nu^2}^{\mathrm{FV}}$, $\mathrm{A}_\nu^{\mathrm{FV}}$ and $\mathrm{A}_S^{\mathrm{FV}}$ functions of the quantities $\tilde{\mathrm{M}}^{\mathrm{FV}}$, $\tilde{\mathrm{F}}^{\mathrm{FV}}$, $\tilde{\mathrm{F}}^{\mathrm{UFV}}$ and $\tilde{\Phi}_{LIN}$, whose expressions are written in details in the appendix. Again we can note that equation (51) remains equal to (45) since we apply the FV scheme only in the hyperbolic phase of the problem.

The dispersion relation (53) produces the relative error w.r.t. (42) sketched in figure 6. From the comparison we can observe that, even though the dispersion error grows as kh_0 increases, for low values of kh_0 the scheme provides the same dispersion accuracy of the FD4 scheme.

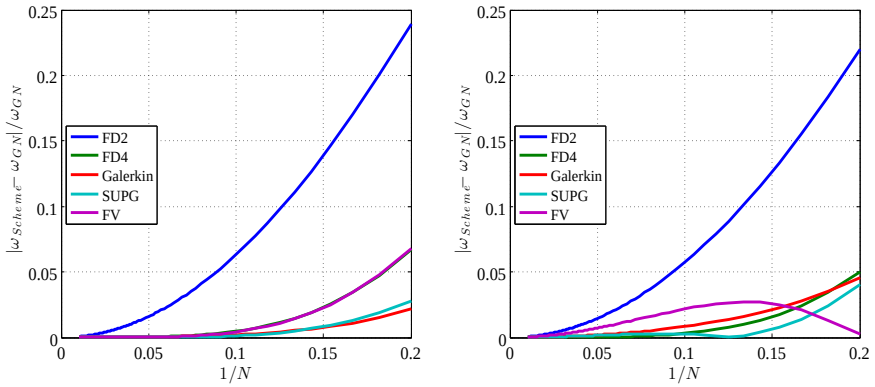

Figure 6: Dispersion error for the FV scheme for $kh_0 = 0.5$ (left) and $kh_0 = 2.5$ (right): comparison w.r.t. the FD2, FD4, Galerkin and SUPG schemes.

Finally, figure7 shows the effects of the 4 different configurations on the discretization of the elliptic problem. Looking to the picture we can observe, again, that the several configurations provide very close dispersion errors when $kh_0 = 0.5$, while their accuracy diverges significantly for $kh_0 = 2.5$ and the best description is given, also in this case, by the configuration 4.

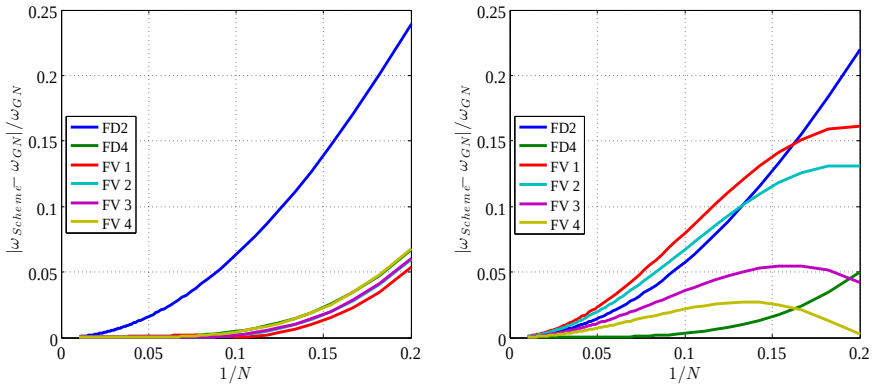

Figure 7: Dispersion error for the FV scheme for $kh_0 = 0.5$ (left) and the $kh_0 = 2.5$ (right): comparison among the different configurations possible for the elliptic phase solution.

In conclusion, studying the dispersion properties of the two formulations proposed, we found that, although the choice to lump or not the Galerkin mass matrix does not affect the general accuracy of the scheme on the elliptic phase but it strongly affects its dispersion properties, especially for higher values of

kh_0. Among the several degrees of freedom, the choice of not lumping any of the mass matrices of the elliptic problem, allows the schemes to give the best accuracy. Moreover, both the FE and FV approaches provide a dispersion description close (FV) or even better (FE) to the one of a fourth order scheme for low values of kh_0 (shallow waters). As kh_0 increases (deep waters) the error tends to increase for the FV scheme, still remaining better w.r.t. a second order one, while remains very low for the SUPG scheme.

5.2 Time discretization : space continuous analysis

We consider now the analysis of the dispersion of the schemes in time. This analysis should be performed on the linearized system, but it can be greatly simplified by exploiting the reformulation of the equations used here.

We start by assuming that at a given time $t = t^*$ we have for a Fourier mode

$$\begin{pmatrix} \phi \\ u \\ \eta \end{pmatrix} = \begin{pmatrix} \hat{\phi}(t^*) \\ \hat{u}(t^*) \\ \hat{\eta}(t^*) \end{pmatrix} e^{j\kappa x} .$$

Setting $c^2 = gh_0$, and $\mu = \kappa h_0$, we can use now (43) to deduce for a Fourier mode in space

$$\phi = j\kappa c^2 \frac{\mu^2/3}{1+\alpha\mu^2/3}\eta$$

so that the Fourier symbol for the last in (44) is (dropping for simplicity the dependence on t^*)

$$c^2\eta_x - \phi = j\kappa c^2(1 - \frac{\mu^2/3}{1+\alpha\mu^2/3})\eta$$

The last expression, however, is also obtained as the Fourier symbol obtained from the equivalent PDE

$$q_t + a^2\eta_x = 0\,,$$

having set $\partial q = h\partial u$, and

$$a(\mu) = c\sqrt{1 - \frac{\mu^2/3}{1+\alpha\mu^2/3}} \tag{54}$$

Indeed, the dispersion relation (42) of the full Green-Naghdi system is trivially obtained from that of the "dispersion equivalent system"

$$\begin{aligned} \eta_t + q_x &= 0 \\ q_t + a^2\eta_x &= 0 \end{aligned}$$

It can be easily cheched that for this system $\omega^2 = \kappa^2 a^2$, which reduces to (42) with definition (54). In particular, we see from this definition that stability the condition $\alpha \geq 1$ is necessary for the well-posedness of this analogy. So, to analyze the time discretization, we will use the ordinary differential system obtained from these equivalent PDEs, namely

$$\frac{d}{dt}\mathbf{U} = \mathcal{L}(\mathbf{U}) = -j\kappa \begin{pmatrix} q \\ a^2\eta \end{pmatrix} = -j\kappa A\mathbf{U}$$

having set $\mathbf{U} = (\eta,\ q)^t$. The matrix A is real valued, and has real eigenvalues and linearly independence eigenvectors :

$$A = \begin{pmatrix} 0 & 1 \\ a^2 & 0 \end{pmatrix} = \underbrace{\begin{pmatrix} 1 & 1 \\ -a & a \end{pmatrix}}_{R_A} \begin{pmatrix} -a & 0 \\ 0 & a \end{pmatrix} \underbrace{\frac{1}{2}\begin{pmatrix} 1 & -1/a \\ 1 & 1/a \end{pmatrix}}_{L_A}$$

Due to the properties of A, and to the linearity of the schemes, we can analyze the behaviour of the discretizations considered on any of the scalar "characteristic variables" defined by

$$\mathbf{W}_A = L_A \mathbf{U}$$

In other words, we can finally use standard techniques applied to the ordinary differential equation

$$\dot{w} + \lambda w = 0$$

with $\lambda = \pm j\kappa a(\mu)$.

This analysis is classical : the ODE is discretized, and the discrete values of w are formally replaced by samples of complex oscillating mode $w^n = w_0 e^{\nu t^n}$, with $\nu = \xi + j\omega$. The phase ω and the amplification rate ξ are then obtained by solving the algebraic equations for $\rho = e^{\nu \Delta t}$ associated to each scheme. The interested reader can refer to [**?**] for details.

The results are summarized in figures 8 and 9. The fist figure shows the overall behaviour of the semi-discrete phase for the three schemes (AM4 on the top row, eBDF3 in the middle row, and RK3 on the bottom). An extremely good approximation of the dispersion relation is obtained with the RK3 scheme, while we bserve a classical behaviour with the multistep schemes (AM4 and eBDF3) showing three modes : a physical one extremely close to the exact dispersion relation of the Green-Naghdi system, and two spurious ones. The amplification rates associated to these modes behave as expected : there is practically no dissipation on the physical mode, while the spurious modes are strongly dissipated.

A more quantitative comparison is shown in figure 9. In the figure, the dependence of the error on the number of points per wavelength is reported. Note that to obtain these plots we have used the relations $N = \lambda/\Delta x$, $\lambda\kappa = 2\pi$ and the CFL condition $\Delta t = CFL\Delta x/c$ to obtain

$$\kappa \Delta t = \frac{\mathrm{CFL}}{c}\frac{2\pi}{N}$$

with the maximum allowed CFL used for each scheme. As for the time-continuous analysis, we report the errors for a long wave ($\mu = 0.5$) and for a shorter wave with $\mu = 2.5$.

The figures shows that in both cases the eBDF3 provides the smallest dispersion error, which may be influential useful when considering very long time propagation. In both cases, the AM4 scheme is the one providing the worst results. The number of points to go below a 5% error may is estimated to less than 5 for eBDF, 8 for the RK3 for the short wave (6 or 7 for a long wave), and about 15 for AM4 (reduced to 8 for a long wave). The errors of the RK3 and eBDf3 are quite low, and anyways comparable to those obtained with in the time continuous analysis. The error of the AM4 scheme is somewhat higher. This is however compensated by the slightly higher efficiency of the method (less right hand side evaluations for a given final simulation time).

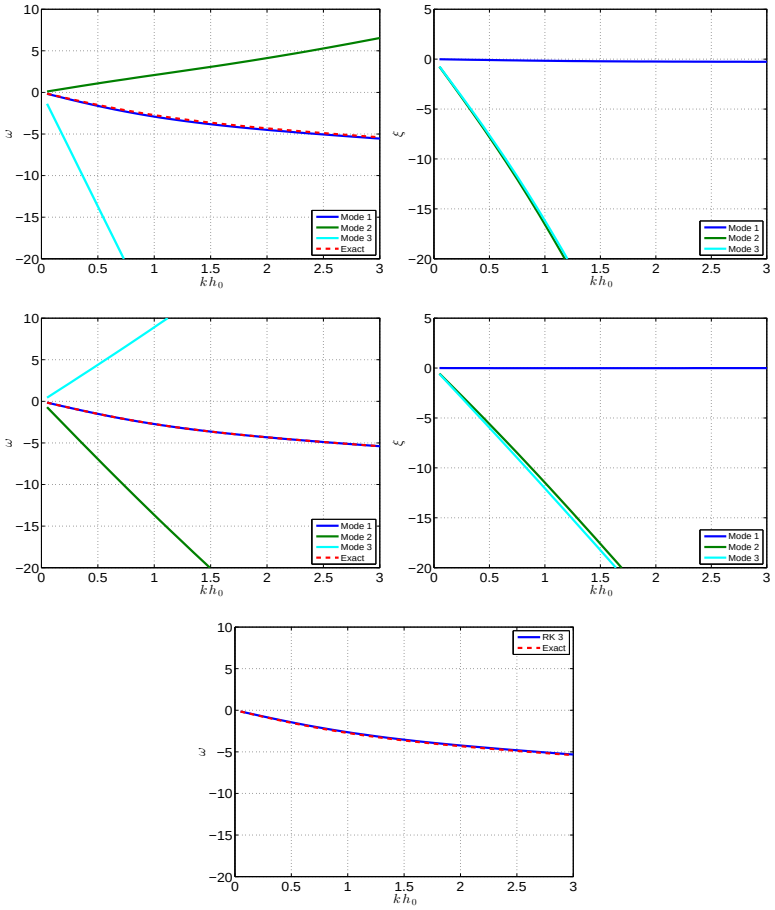

Figure 8: Dispersion error of the time discretizations : overview. Top : AM4 scheme. Middle : eBDF3 scheme. Bottom : RK3 scheme.

6 Embedding wave breaking

Wave breaking is an important modelling issue in near-shore environments. It dissipates wave energy through the generation of turbulence, including substantial air entrainment. As wave shoal, wave fronts become steeper and steeper, until wave's crest overturns. Depth averaged equations are unable to describe this phenomenon and an additional physical closure for wave breaking is necessary, to simulate the breaking process numerically. The closure model is composed of two main elements : a trigger mechanism related to the initiation and possibly the termination of the breaking process ; an energy dissipation mechanism. In this work, as in [54, 25, 2], the breaking dissipation is included by reverting locally to the non linear shallow water (NLSW) equations and letting breaking fronts converge into moving bores or hydraulic jumps. The total energy dissipation through these features is used as a model for wave breaking dissipation. Such an approach leads to hybrid models and has gained attention by several researchers in the past few years, please refer to [9, 55, 56, 24, 50, 47, 41, 54, 57].

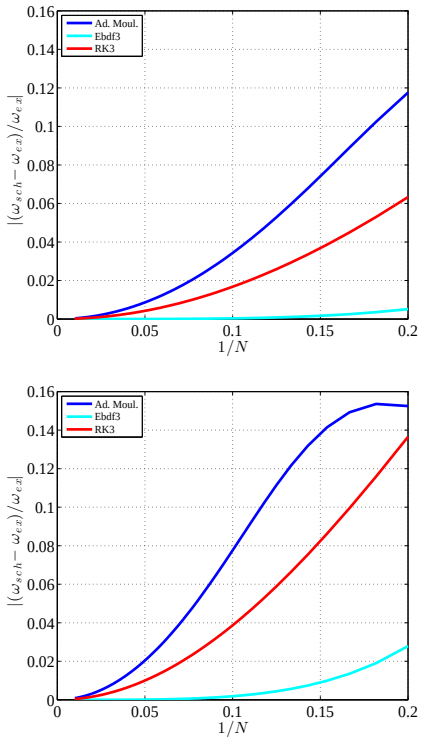

Figure 9: Dispersion error of the time discretizations : dependence on the number of points per wave-length. Left : $\mu = \kappa h_0 = 0.5$ (long wave). Right : Left : $\mu = \kappa h_0 = 2.5$ ("short" wave).

In the solution procedure proposed here, this can be embedded quite simply by setting ϕ to zero in (7). However, we will also test a tighter coupling of the hyperbolic and elliptic phases, by taking into account the presence of breaking regions also in the latter. More details concerning the detection and triggering of the breaking model, and on the coupling between Green-Naghdi and NLSW equations are discussed hereafter.

6.1 Breaking front detection

As a trigger mechanism to determine the initiation and termination of breaking process we use the combination of physical criteria presented in [25] :

- the surface variation criterion: $\partial_t \eta \geq \gamma\sqrt{gh}$, with $\gamma \in [0.3,\ 0.65]$ depending on the type of breaking ;
- the local slope angle criterion: $||\nabla\eta||_2 \geq \tan(\phi_c)$, where ϕ_c is the critical front slope at breaking, and $\phi_c \in [14^o,\ 33^o]$ depending on the type of breaking.

The first criterion flags for breaking when $\partial_t \eta$ is positive, as breaking starts on the front face of the wave and has the advantage that can be easily calculated

during the running of the code. The second criterion acts complementary to the first one and is based on the critical front slope approach in [48, 51]. This allows to flag steady hydraulic jumps, while the first is more effective for moving fronts.

As discussed in [25, 54], the different breaking waves are distinguished, and each one is processed individually. In particular, for each front one computes peak and trough depths, h_{peak} and h_{trough} respectively. If the critical Froude number defined by

$$\text{Fr} = \sqrt{\frac{-1 + (1 + 2h_{\text{peak}}/h_{\text{trough}})^2}{8}}$$

is larger than a certain threshold, typically $\text{Fr}_c \approx 1.3$, then a breaking region is defined, centered around the point of maximum slope and of width $l_{\text{NLSW}} \approx 7.5(h_{\text{peak}} - h_{\text{trough}})$. All the nodes within this region are breaking nodes. For breaking nodes, the shallow water equations are solved. The modifications to the numerical model made to achieve this coupling are discussed in the next paragraph. More details on wave breaking detection can be found in [25, 54] and references therein.

6.2 Numerical treatment of breaking regions

In the region flagged as breaking, the flow quantities are evolved using the shallow water equations. We will compare in our results two different approaches

1. Simply neglect the terms related to ϕ in the spatial discretization. For a breaking node i, this means setting $\overline{\mathbf{\Phi}}_i = 0$ in (16), or (30). In this case, the two phases of the discretization (elliptic and hyperbolic) are completely independent on one another. In particular, only the hyperbolic phase is aware of the breaking process ;

2. To have a tighter coupling between the two phases, and hopefully a smoother transition, the breaking condition is embedded in the elliptic phase as a sort of Dirichlet boundary condition. In particular, for a breaking node i the line of the matrix issuing form the finite element discretization discussed in section §3.2 is replaced by $\delta_{ij}\Delta x$, δ_{ij} denoting Kroenecker's δ, while the right hand side is set to zero. The elliptic problem being second order, the discrete solution for ϕ is now expected to go to zero in breaking nodes trying to keep also the continuity of its first derivative. As the source term $\overline{\mathbf{\Phi}}$ is kept into the discretization, and as it involves an average of neighbouring values of ϕ, a smoother transition may be expected.

In both cases, the nonlinear limiters involved in the discretizations are turned on only if the nodes are breaking. In other words, in non breaking regions we set $\psi = 1$ in both (18) and (29).

7 Numerical tests and results

7.1 Convergence

In order to verify the implementation of our models we perform a grid convergence analysis for a propagation of a solitary wave of $\epsilon = 0.2$ over an undisturbed

bed of $h_0 = 1m$. The domain is of $200m$ $[-100,\ 100]$ the and the initial wave was placed in $x_0 = -50m$. The error $E(\eta)$ in the L^2 norm, is computed by comparing the numerical results with the analytical solution after the wave has traveled for $30sec$. The partitions used for the tests are $dx = 0.2, 0.1, 0.05, 0.025m$. Figure 10 shows the grid convergence results for the FV scheme the FE schemes (SUPG and Galerkin) and for all the time discretizations. The slopes obtained from the error reveals a convergence with more than a third order of accuracy in space, for all the models in time and for all the schemes.

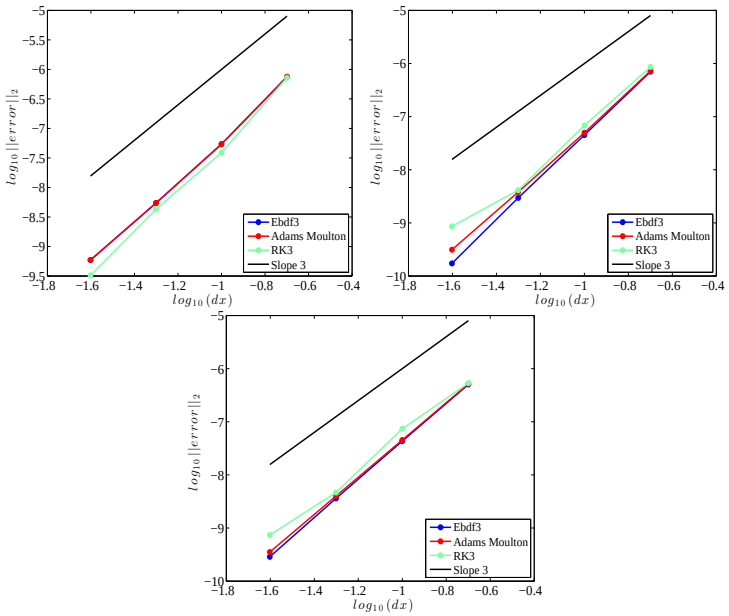

Figure 10: Convergence rates for the FV scheme (left) the SUPG scheme (center) and the Galerkin scheme (right)

7.2 Periodic wave propagation over a submerged bar

The next test case is the periodic wave propagation over a bar. The classical tests of Beji and Battjes [4] examine sinusoidal wave propagation over a submerged bar as to investigate the frequency dispersion characteristics and nonlinear interaction of complex wave propagation phenomena. The experiments were conducted in a $37.7m$ long, $0.8m$ wide, and $0.75m$ high wave flume. A hydraulically driven, piston-type random wave generator was located at the left side of the flume and a $1:25$ plane beach with coarse material was placed at the right side to serve as a wave absorber. The submerged trapezoidal bar was $0.3m$ high with front slope of $1:20$ and lee slope of $1:10$ separated by a level plateau $2m$ in length. For the numerical test case, the wave-making internal source function is placed at $x = 0m$ and the dimension of the computational domain is set to $x \in [-10, 29m]$. Sponge layer widths are set to $L_s = 5m$ at both ends of the computational domain. For the computation $dx = 0.04m$ and the CFL number used is equal to 0.2.

Case (a): First we consider the test case with $A = 0.01m$ incident wave amplitude and $T = 2.02s$ wave period. The water depth parameter is $kh_0 \approx 0.67$ with depth to wavelength ratio $h_0/L = 0.11m$. The propagating waves shoals along the front slope of the bar causing the growth of the wave amplitude and the surface profile to become asymmetric. In the back slope the waves break up into independent waves which travel at their own speed. Figure 11 presents the comparison between experimental data and numerical ones, produced using the FV scheme, recorded in wave gauges for all the time schemes used in this work. Figures 12 and 13 presents the same for the Galerkin and the SUPG schemes respectively. We must mention that the wave signals have been phase calibrated according to gauge 4. For brevity we only consider gauge 4 placed at the toe of the bar, gauge 7 placed before the plateau of the bar, gauge 8 placed on the top of the bar and gauge 10 placed after the bar.

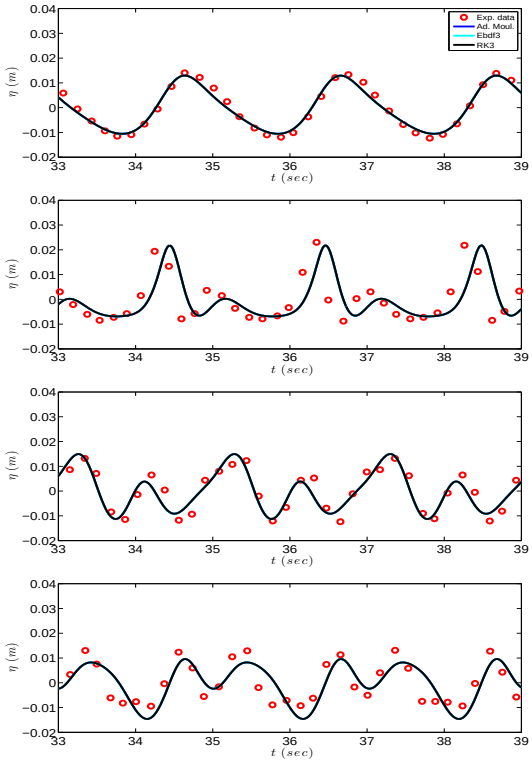

Figure 11: Time series of surface elevatio, for the FV scheme, at wave gauges 4,5 (up) 8,10 (down) for periodic wave propagation over a bar

We can observe that the three scheme produce same results for the gauges before and on the plateau of the bar while there is a slight modification for the gauge in the lee side of the bar. In this region the water depth parameter kh increases rapidly so it is expected form figure 6 that the FV scheme produces less accurate results since the dispersion error is higher as k grows.

Case(b): In this case wave breaking is expected to occur at the end of the first slope and after the shoaling of the waves. The waves height is of $0.054m$

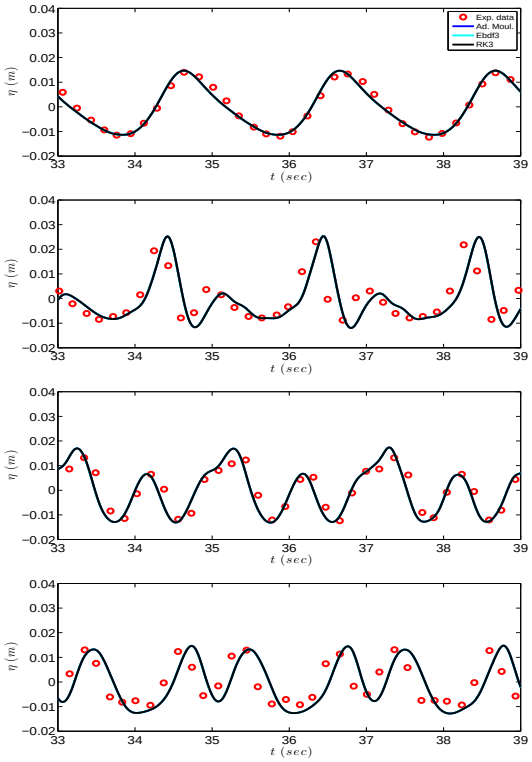

Figure 12: Time series of surface elevation, for the Galerkin scheme, at wave gauges 4,5 (up) 8,10 (down) for periodic wave propagation over a bar

and the wave period is $T = 2.5s$, that corresponds to the water depth parameter $kh_0 \approx 0.52$, with depth to wavelength ratio of $h/L = 0.0835$. The value of the surface breaking criterion γ, for the wave breaking mechanism, is set to 0.3. We muse denote that for the numerical treatment of the wave breaking (in all the test cases), we use the second approach described in section §6.2. A discussion on the topic will follow. The numerical results along with the experimental data are recorded in four wave gauges (1 to 4) which were placed at $x = 6, 12, 13$ and $14m$ respectively. The are all presented in figures 14 and 15 for the FV and the SUPG schemes respectively.

The wave shape is well-reproduced for all wave gauges. As expected the waves shoal along the front slope, since nonlinear effects cause the waves propagating along this slope to steepen and broke at the beginning of the bar crest. Breaking is classified as plunging. Bound higher harmonics are developed along the front slope, which are then released from the carrier frequency on the lee side of the bar as the water depth parameter kh increases rapidly. Figures 16 and 17 illustrates the wave-by-wave treatment and the l_{NLSW} area along the centerline for FV and SUPG schemes respectively, at different time instances (covering roughly one wave period). The time scheme used for both models was Adams Moulton but similar results can be obtained using the other time schemes. The onset of breaking is correctly predicted for both schemes, close

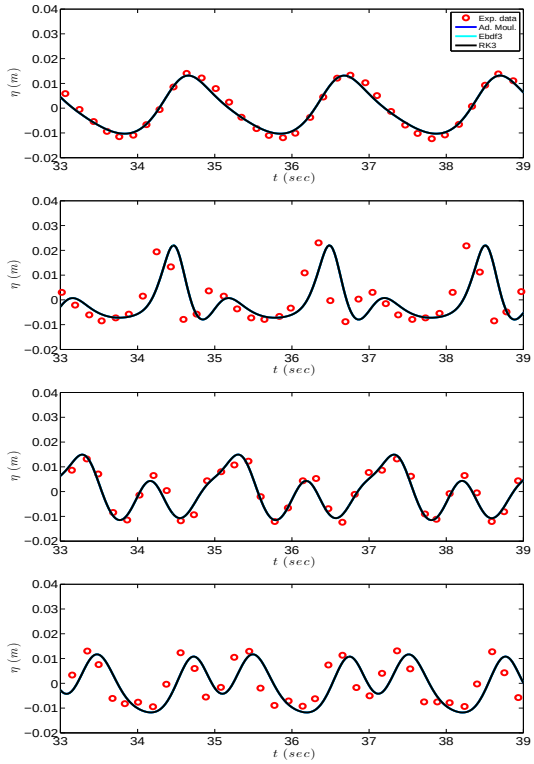

Figure 13: Time series of surface elevation, for the SUPG scheme, at wave gauges 4,5 (up) 8,10 (down) for periodic wave propagation over a bar

to the beginning of the bar crest and continues along the flat of the bar leading to a wave height decay. We can observe that during the breaking process the SUPG scheme is more diffusive leading to a slightly earlier termination of the procedure and after that a small amplification of the wave height compared to the FV scheme. Different particularization for the breaking model maybe needed for different numerical models but this study is beyond the purpose of this work.

7.3 Solitary wave runup on a plane beach

As to verify and validate our implementations, we use one of the most intensively studied problems in long-wave modeling, the solitary wave-run up on a plane beach. Synolakis [52] carried out laboratory experiments for incident solitary waves of multiple relative amplitudes, in order to study propagation, breaking and run-up over a planar beach with a slope 1:19.85. Detailed description of the test case, along with the initial conditions, can be found for example in[52, 7, 56, 47, 17] among many others. The incident wave height used in this work is $A/h = 0.28$ with $h = 1m$. This wave breaks strongly both in the run-up and the run-down phases of the motion. The computational domain used is $x \in [-20,\ 100m]$ with $dx = 0.05m$. The CFL number is set equal to 0.2, a

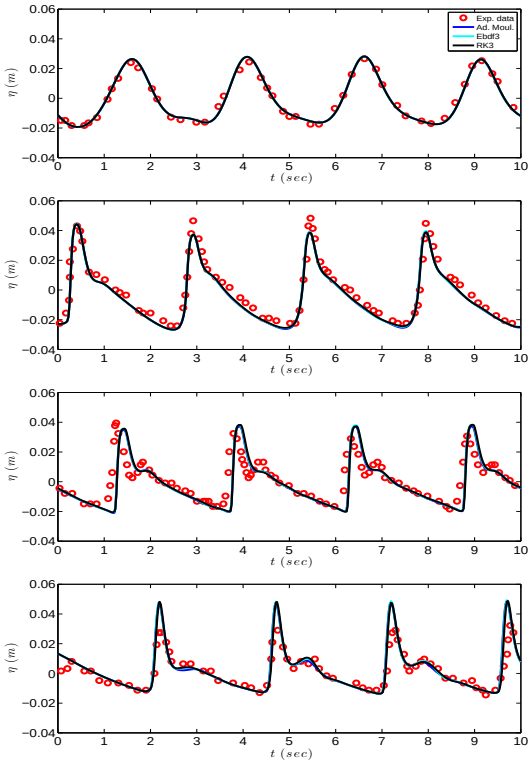

Figure 14: Time series of surface elevation, for FV scheme, at wave gauges for periodic wave propagation over a bar

sponge layer is applied offshore with length $L_s = 5m$ and γ is set equal to 0.6. Finally, a Manning coefficient of $n_m = 0.01$ is used to define the glass surface roughness used in the experiments.

We perform this test case using all the time schemes described up to now. Like the periodic wave propagation over a bar, we obtain the same results for the different time schemes. For brevity, only two snapshots of the comparison are presented in figure 19. Since we show that all the time schemes used up to now lead us to the same results, from now on, the presented results will use Adams Moulton time scheme unless otherwise said. Of course the choice of the above time schemes is not restricted and any time scheme of order greater than three can be used. Figure 18 compare the measured surface profiles and the numerical model's results on different non-dimensional times. Blue line denotes the numerical results produced by the FV scheme, green dotted line the results given by the SUPG scheme and red circles denote the experimental data.

Until time $t\sqrt{g/h} = 10$ the solitary propagates to the shore and the two models produce, as expected, identical results since wave breaking hasn't started yet. The experimental wave, breaks around $t\sqrt{g/h} = 20$. The numerical solution is represented like a bore storing the water spilled from the breaking wave behind the front. A slight difference can be seen in the two solutions at time $t\sqrt{g/h} = 20$ which is due to the usage of two different limiters. SUPG scheme

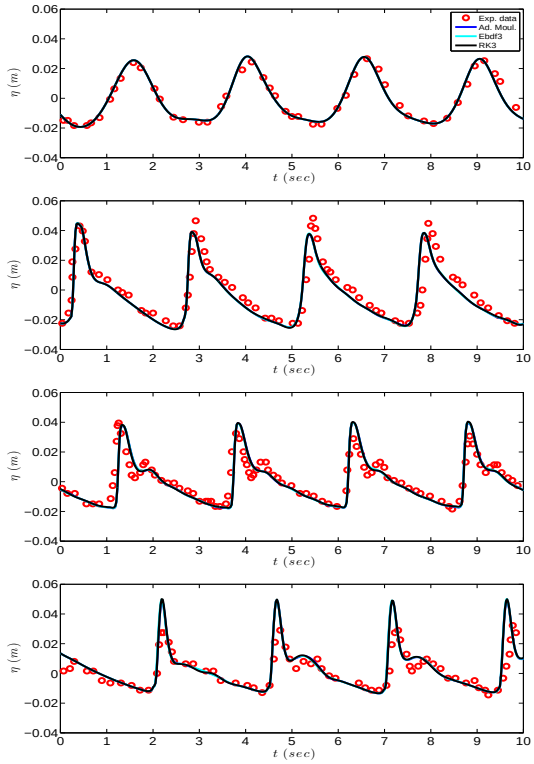

Figure 15: Time series of surface elevation, for FE scheme, at wave gauges for periodic wave propagation over a bar

uses the smooth sensor limiter while FV scheme uses the minmode limiter. Usage of different limiters produces different results in the wave breaking region but this study is beyond the scope of this work. At time $t\sqrt{g/h} = 25$ the bore collapses at the shore and the results shows really good agreement. After that the wave starts to run-up. The time of maximum run-up occurs at $t\sqrt{g/h} = 45$. During the backwash a breaking wave is created at $t\sqrt{g/h} = 55$ near the still water level. The numerical solution is approximated as a hydraulic jump for both models which can be fully resolved since the breaking criterion recognize it and the NLSW equations are used in this region.

7.4 Solitary wave on a composite beach

One of the benchmark methods for tsunami model validation and verification according to the NOOA center for tsunami research is the problem the propagation of a solitary wave over a composite beach which simulates the Revere beach in Massachusetts. A physical model was constructed at the Coastal Engineering Research Center in Vicksburg, Mississippi by the U.S. Army Corps of Engineers. The configuration of the problem can be found in [35, 53]. The setup of the problem is shown in figure 20. The wave gauges, where the time series of the surface elevation is examined, are placed at $x = 15.04, 17.22, 19.04, 20.86, 22.33, 22.80m$.

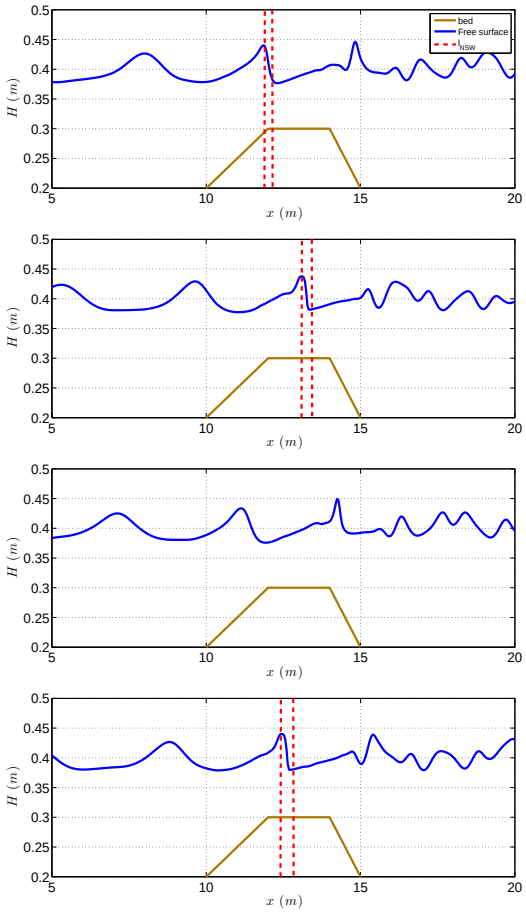

Figure 16: Spatial snapshots, for FV scheme, along the centerline of regular waves breaking over a bar with the flow between two consecutive vertical lines governed by the NSW equations

Two cases are implemented and tested in this work. The first one is the propagation and breaking of a solitary wave of $\epsilon = 0.3$ and the second one involves a solitary wave of higher non-linearity of $\epsilon = 0.7$. The computational domain used is of $27.23m$, $x \in [-5,\ 23.23]$, with the initial solitary placed at $x = 0m$ and $h_0 = 0.218m$. The CFL number is set to 0.2 and $dx = 0.046m$. A sponge layer of $2m$ is placed at the left boundary while a vertical wall is placed at the right boundary. For the surface variation criterion , γ is set equal to 0.6.

Figure 21 shows the comparison between the experimental data (red circles) and the numerical results. Again, blue line denotes the numerical results produced by the FV scheme while green dotted line denotes the results given by the SUPG scheme. The solitary travels down the domain, shoals and break between the second and the third wave gauges. After breaking it continues to travel onshore until it hits the wall, reflects and starts to propagate offshore. We observe a very good match between the experimental data and the numerical

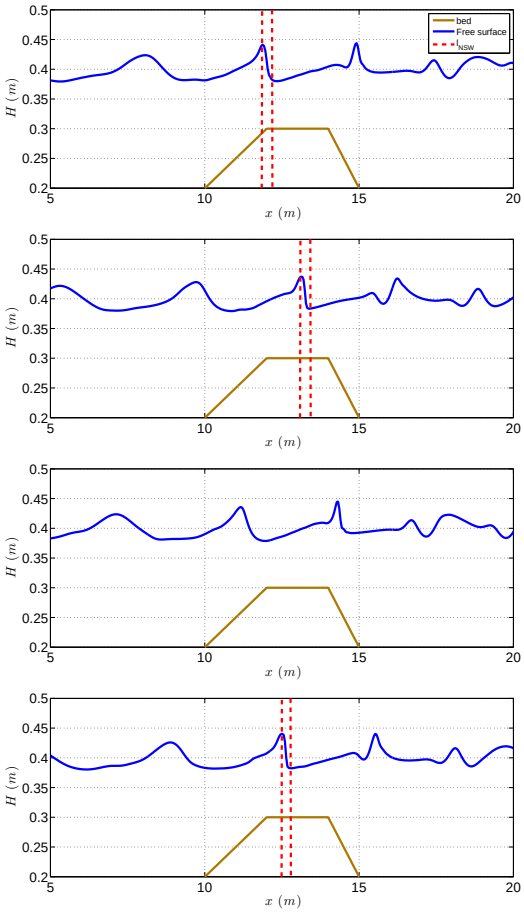

Figure 17: Spatial snapshots, for SUPG scheme, along the centerline of regular waves breaking over a bar with the flow between two consecutive vertical lines governed by the NSW equations

results for almost all the wave gauges.

In figure 22 the numerical results along with the experimental data for the second case ($\epsilon = 0.7$) are presented. The solitary wave is highly non-linear and presents the same behavior. It breaks between the second and the third wave gauges, reflects on the wall and travels offshore. The numerical results are in agreement with the experimental data. We must notice that after the reflection of the solitary, the numerical results produced by the FV scheme are slightly ahead compared to the ones produced by the SUPG scheme and the experimental data.

7.5 Solitary wave propagation over a two-dimensional reef

The last experimental test case is on solitary wave transformations over an idealized fringing reef and examines the model's capability in handling non-linear dispersive waves along with wave breaking and bore propagation. It

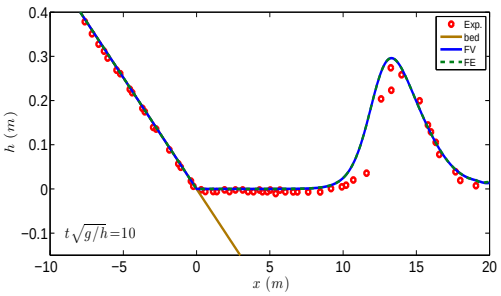
Exp.
bed
FV
FE
$h\ (m)$
$t\sqrt{g/h}$=10
$x\ (m)$

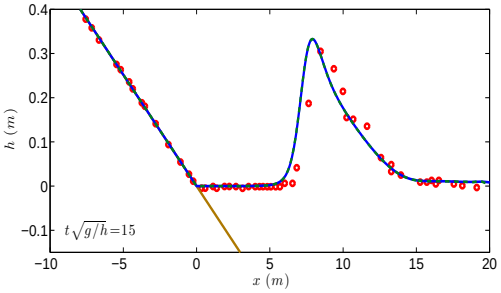
$h\ (m)$
$t\sqrt{g/h}$=15
$x\ (m)$

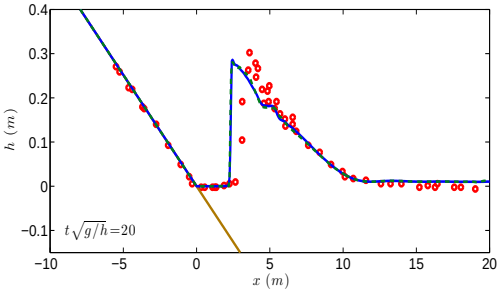
$h\ (m)$
$t\sqrt{g/h}$=20
$x\ (m)$

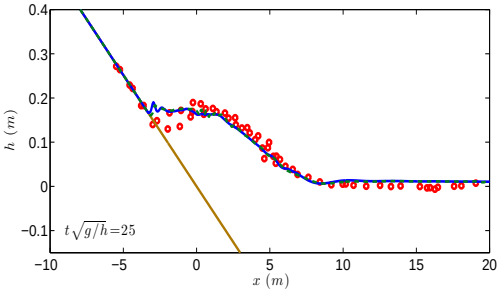
$h\ (m)$
$t\sqrt{g/h}$=25
$x\ (m)$

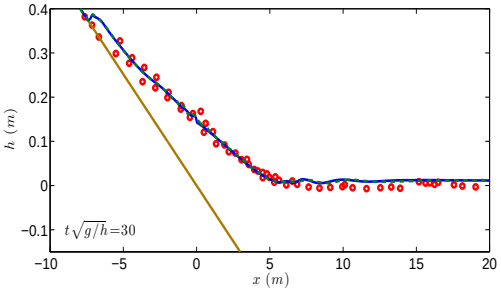
$h\ (m)$
$t\sqrt{g/h}$=30
$x\ (m)$

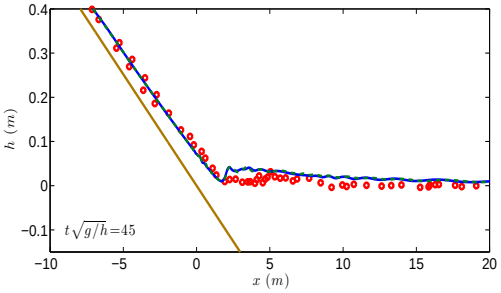
$h\ (m)$
$t\sqrt{g/h}$=45
$x\ (m)$

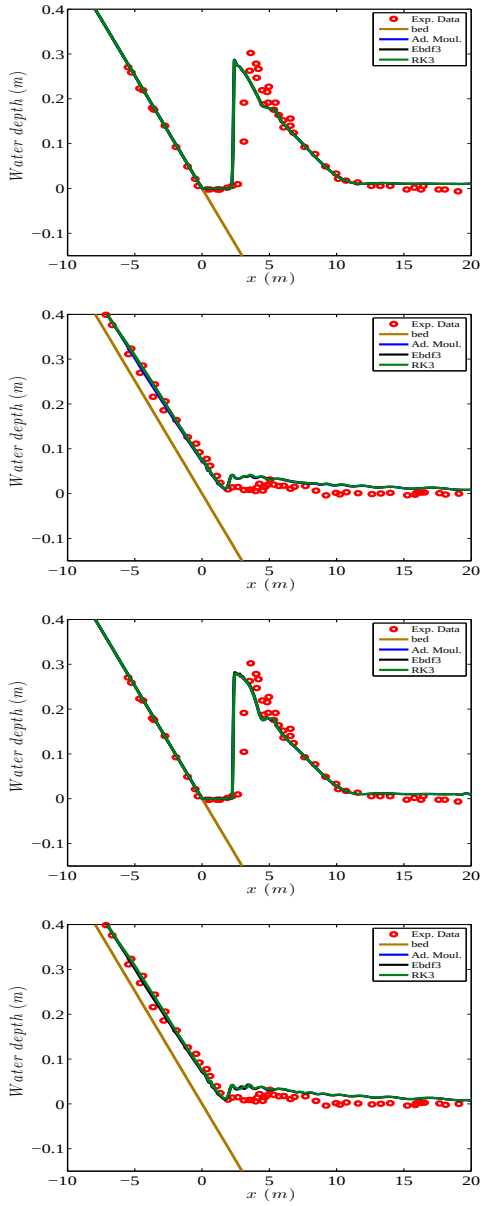

Figure 19: Comparison of different time schemes on a solitary wave run-up on a plane beach, for the FV scheme (up) and the SUPG scheme (down)

was initially presented in [46] and the laboratory experiments carried out at the O.H. Hinsdale Wave Research Laboratory of Oregon state University from 2007-2009. The test includes a steep slope along with a reef crest in order to represent fringing reefs. The topography includes a fore reef slope of 1/12 a $0.2m$ reef crest and a water depth $h_0 = 2.5m$. The reef crest is then exposed by $6cm$ and submerges the flat with $h = 0.14m$. A solitary wave of $0.75m$ high

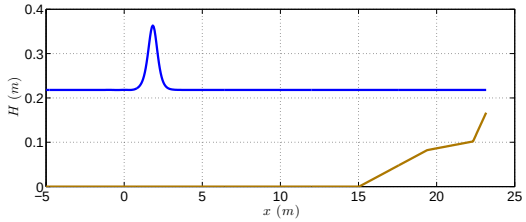

Figure 20: Initial conditions of the solitary wave on a composite beach

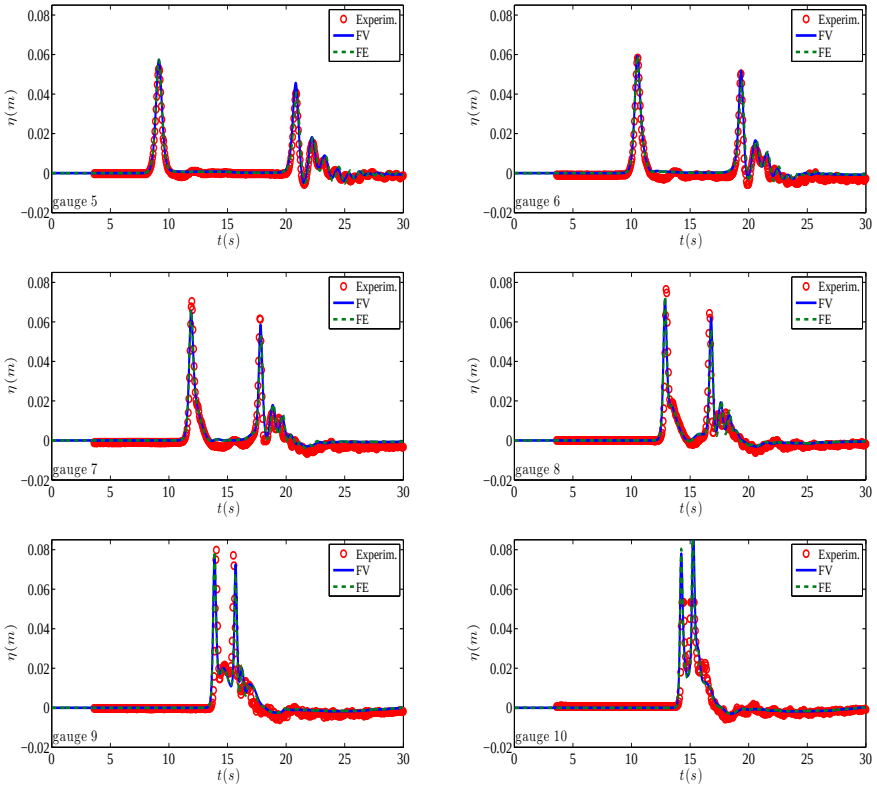

Figure 21: Time series of the free surface elevation at the wave gauges for the solitary of non-linearity $\epsilon = 0.3$

is used as an initial condition. The computational domain is $x \in [0, 83.7m]$ with $dx = 0.1m$. A CFL number of 0.2 is used, and $\gamma = 0.6$. Wall boundary conditions are placed at each boundary of the computational domain and as suggested in [47] a Manning coefficient $n_m = 0.012s/m^{1/3}$ is used to define the roughness of the concrete surface of the reef. Experimental results for the free surface elevation were recorded at 14 wave gauges [46] along the centerline of the computational domain. Figures 23 and 24 compare the measured and computed wave profiles, for both schemes, as the numerical solitary wave propagates. As

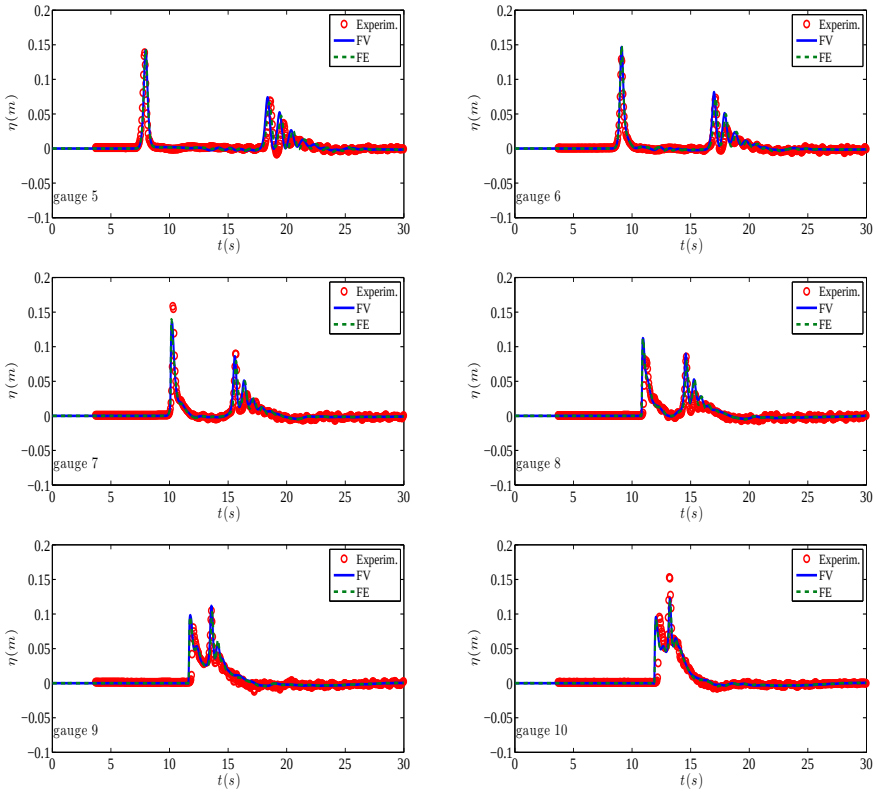

Figure 22: Time series of the free surface elevation at the wave gauges for the solitary of non-linearity $\epsilon = 0.7$

the initially symmetric solitary propagates along the inclined bottom, starts to shoal across the toe of the slope at $x = 25.9m$ and it begins to skew to the front.

The wave begins to break as it approaches the reef, developing a plunging breaker on the top of the reef crest that collapses around $t = 68.5s$. Both models are mimicking the breaker as a collapsing bore that slightly underestimates the wave height but conserved the total mass. The two models give identical results as the wave over tops the reef, deforming both a hydraulic jump and a downstream propagating bore. A difference can be observed in the approximation of the undular bore that forms after the reflection on the wall, over-top the reef and travels offshore. This indicates again that maybe different treatment of the breaking mechanism is needed for different numerical models, but this study is beyond the scope of this work.

7.6 Discussion on two different breaking formulations

As mentioned in section §5.2, in this work, we performed two different approaches concerning the implementation of wave breaking technique in both schemes. The first approach has the advantage that the elliptic and the hyperbolic part are completely independent of one another and only the hyperbolic

phase is aware of the breaking process. This makes it particular easy to implement in any hyperbolic scheme by simply using $\bar{\mathbf{\Phi}}$. In the second approach, we expect to achieve a smother transition between the two phases, but the breaking condition must be embedded in the elliptic part. In this section we use the two different wave breaking formulations in both schemes. We want to reveal the differences, if any, the limitations and advantages of each approach by performing test cases of different wave characteristics and breaking conditions.

The first test case performed is the solitary wave propagation over a plane beach. It was described in section §7.3. Figure 27 shows the numerical results obtained from the two schemes and for both approaches and depicts the breaking procedure before the run-up of the wave. The left column corresponds to the FV scheme and the right column to the SUPG scheme. Each snapshot presents the free surface elevation and $\bar{\mathbf{\Phi}}$. We must mention that while for the FV scheme $\bar{\mathbf{\Phi}}_i$ contributes only to the momentum equation, this is not the case for the SUPG scheme in which $\bar{\mathbf{\Phi}}_i$ is coupled (see eq. 11). For this reason and in all the results from now on, we present only the term contributed to the momentum equation. The numerical results obtained for both schemes are quite similar. We can observe that the first approach of wave breaking, in both schemes, tends to be slightly more oscillatory but without affecting the overall solution.

Next figure describes the same problem but with a refined mesh of 4800 nodes. Here the oscillatory behavior of the first approach is revealed in both schemes but is more pronounced in the FV scheme. Oscillations are produced during breaking and due to the abrupt switching between the two formulations. They travel offshore and they affect the back of the wave. We must mention that the SUPG scheme is more diffusive during breaking due to the different nature of the limiters used, compared to the FV scheme. Further research on the effects of the limiters during breaking is necessary. We observe that the more we refine the mesh the more oscillations on $\bar{\mathbf{\Phi}}$ are observed. These are introduced to the free surface elevation and eventually lead us to a non acceptable solution.

Figure 29 presents the numerical results for a solitary wave of $\epsilon = 0.5$ propagating in the same inclined topography as before. As expected the wave breaks in earlier time and once again the figures depict the strong breaking close to the shore. The same behavior as before is revealed.

On the contrast and for the wave propagation over a bar test case (see figure 30), we observe a different trend. While for the mesh of $dx = 0.04$ there are no big differences observed for the two approaches, for a refined mesh of 4000 nodes a phase lag in the results between two formulation is revealed in the region after breaking, perhaps related to the perturbation disturbing the upstream signal. The results produced by the second formulation are closer to the experimental data.

In conclusion we can say that even though the first formulation has the advantage that the elliptic and hyperbolic parts are completely independent and easy to implement in any formulation, it seems more oscillatory than the second approach which switch-off the dispersion terms in a more smooth way. Of course further research on the topic is in need, which will involve the usage of different discretization schemes and irregular meshes.

8 Conclusions

In this paper, we presented a new discretization strategy for the enhanced GN system of equations [8]. The original system has been rewritten in a lower order form by introducing a new variable ϕ, representing the non-hydrostatic part of the pressure. The structure of the new system (6)-(7) consists of a decoupled hyperbolic/elliptic problem where the hyperbolic part is represented by the NLSW equations plus the new source term ϕ. The system is solved in two independent steps. Firstly and for the computation of ϕ the elliptic part is solved. Secondly, the flow variables are obtained by solving the hyperbolic part. For the hyperbolic part anyone of the numerous numerical techniques already existing in literature can be used. In this work three high order schemes have been used for this purpose: the FV scheme with a third order MUSCL type reconstruction, the classical C^0 Galerkin approximation and the upwind stabilized method developed in [44, 2, 3]. The discretization of the elliptic part arising from the non-hydrostatic term is also carried out in a continuous FE framework. All the schemes implemented are endowed with robustness and stability properties such as positivity, well-balancing and wet/dry interfaces treatment. The theoretical analysis of the linear dispersion error of the schemes show an accuracy comparable or even better w.r.t. that of the standard fourth order finite differencing.

The fourth order Adams Bashforth - Adams Moulton method [60, 46], the three stages third order SSP Runge-Kutta scheme [19] and the third order explicit backward differencing method [23] have been used for the integration in time. The substantial equality of the results performed with all the time schemes denotes the general content of the proposed treatment .

Further more a preliminary study on two different formulations on the treatment of the hybrid breaking technique, used here, is also performed. The first approach simply neglects the non-hydrostatic terms having the advantage that the two phases of the discretization are completely independent on one another but the limitation is that nonphysical oscillations appear. The second one has tighter coupling between the two phases leading to a smoother transition and makes it more appropriate for finer meshes.

The numerical models were validated against standard test cases of non-breaking and breaking wave propagation over variable topographies with emphasis to comparisons with experimental results. In all test cases, the presented results were in good agreement with experimental data and previously published solutions.

The flexibility and general features of the presented method makes it appropriate for a multidimensional extension using arbitrary unstructured meshes. Of course for the hyperbolic part either FV, residual distribution or discontinuous Galerkin methods can be used. Furthermore any existing non-linear shallow water code can be modified in this way as to include dispersion characteristics due to the complete independence of the elliptic part. Moreover other numerical schemes could be implemented and tested as well. For example continuous Galerkin for the elliptic part and discontinuous Galerkin for the hyperbolic part to minimize the matrix sizes in hyperbolic step w.r.t full discontinuous Galerkin. For the time integration schemes efficient multi-stage/step time stepping methods can be used.

Acknowledgments

Work partially funded by the TANDEM contract, reference ANR-11-RSNR-0023-01 of the French *Programme Investissements d'Avenir*.

Appendix A1

We report here the definitions of the several quantities called in section §5 and involved in the analysis of the dispersion properties of the schemes. Moreover, the paragraph contains the expressions of the dispersion relation formulae of the FD2 and FD4 schemes used as comparison in figures from 2 to 7 and the description of the several configurations (from 1 to 4) taken into account for the elliptic problem discretization.
The tensors involved in the Galerkin scheme dispersion relation (47) come from:

- the Galerkin mass matrix: $\tilde{\mathrm{M}}^{\mathrm{G}} = \frac{1}{6}\Big(4 + 2\cos\bar{\mu}\Big)$;
- the solution of the elliptic problem: $\tilde{\Phi}_{LIN} = -\frac{gh_0^3}{3}\tilde{\mathrm{T}}^{\mathrm{G}}\Big(\tilde{\mathrm{M}}^{\mathrm{G}}\Big)^{-1}\Big(\tilde{\mathrm{M}}^{\mathrm{G}} - \frac{\alpha h_0^2}{3}\tilde{\mathrm{S}}^{\mathrm{G}}\Big)^{-1}$

and the Galerkin discretization of:

- the first order space derivatives $\partial_x(\cdot)$: $\tilde{\mathrm{F}}^{\mathrm{G}} = j\frac{k}{2\bar{\mu}}\Big(2\sin\bar{\mu}\Big)$;
- the second order space derivatives $\partial_{xx}(\cdot)$: $\tilde{\mathrm{S}}^{\mathrm{G}} = \frac{k^2}{\bar{\mu}^2}\Big(2\cos\bar{\mu} - 2\Big)$;
- the third order space derivatives $\partial_{xxx}(\cdot)$: $\tilde{\mathrm{T}}^{\mathrm{G}} = j\frac{k^3}{2\bar{\mu}^3}\Big(2\sin 2\bar{\mu} - 4\sin\bar{\mu}\Big)$;

where $\bar{\mu} = k\Delta x$ and k represents the wavenumber associated to the Fourier mode.

The dispersion relation (50) of the SUPG scheme involves the two other quantities:

- $\tilde{\mathrm{M}}^{\mathrm{UFE}} = j\sin\bar{\mu}$
- $\tilde{\mathrm{F}}^{\mathrm{UFE}} = \frac{k}{\bar{\mu}}\Big(2\cos\bar{\mu} - 2\Big)$

which derive from the FE discretization of the upwind flux.

Concerning the FV scheme (53) we define the following set of tensors which comes from the discretization of the:

- elliptic term $\overline{\overline{\mathbf{\Phi}}}$: $\tilde{\mathrm{M}}^{\mathrm{FV}} = \frac{1}{6}\Big(6 + 2\cos\bar{\mu}\Big)$

- centered fluxes: $\tilde{\mathrm{F}}^{\mathrm{FV}} = j\dfrac{k}{2\bar{\mu}}\left(\dfrac{8}{3}\sin\bar{\mu} - \dfrac{1}{3}\sin 2\bar{\mu}\right)$
- upwind fluxes: $\tilde{\mathrm{F}}^{\mathrm{UFV}} = \dfrac{k}{2\bar{\mu}}\left(\dfrac{4}{3}\cos\bar{\mu} - \dfrac{1}{3}\cos 2\bar{\mu} - 1\right)$

Figures from 2 to 7 show the dispersion errors of the several schemes w.r.t. the analytical dispersion relation of the model given by (42). The comparison is made for low and high values of the parameter kh_0 w.r.t. the errors provided by the FD2 and FD4 discretization schemes, whose dispersion relations are respectively:

$$\left(\omega_h^{\mathrm{FD2}}\right)^2 = gh_0\left(\tilde{\mathrm{F}}^{\mathrm{FD2}}\right)^2 - \tilde{\mathrm{F}}^{\mathrm{FD2}}\tilde{\Phi}_{LIN}^{(FD2)} \tag{55}$$

$$\left(\omega_h^{\mathrm{FD4}}\right)^2 = gh_0\left(\tilde{\mathrm{F}}^{\mathrm{FD4}}\right)^2 - \tilde{\mathrm{F}}^{\mathrm{FD4}}\tilde{\Phi}_{LIN}^{(FD4)} \tag{56}$$

$$\tag{57}$$

where the introduced tensors are defined in the following and come from the second order finite difference:

- discretization of the first order space derivatives $\partial_x(\cdot)$: $\tilde{\mathrm{F}}^{\mathrm{FD2}} = \tilde{\mathrm{F}}^{\mathrm{G}}$
- discretization of the second order space derivatives $\partial_{xx}(\cdot)$: $\tilde{\mathrm{S}}^{\mathrm{FD2}} = \tilde{\mathrm{F}}^{\mathrm{G}}$
- discretization of the first order space derivatives $\partial_{xxx}(\cdot)$: $\tilde{\mathrm{T}}^{\mathrm{FD2}} = \tilde{\mathrm{F}}^{\mathrm{G}}$
- solution of the elliptic problem: $\tilde{\Phi}_{LIN}^{(FD2)} = -\dfrac{gh_0^3}{3}\tilde{\mathrm{T}}^{\mathrm{FD2}}\left(1 - \dfrac{\alpha h_0^2}{3}\tilde{\mathrm{S}}^{\mathrm{FD2}}\right)^{-1}$

and from the fourth order finite difference:

- discretization of the first order space derivatives $\partial_x(\cdot)$: $\tilde{\mathrm{F}}^{\mathrm{FD4}} = j\dfrac{k}{12\bar{\mu}}\Big(-2\sin 2\bar{\mu} + 16\sin\bar{\mu}\Big)$
- discretization of the second order space derivatives $\partial_{xx}(\cdot)$: $\tilde{\mathrm{S}}^{\mathrm{FD4}} = \dfrac{k^2}{12\bar{\mu}^2}\Big(-2\cos 2\bar{\mu} + 32\cos\bar{\mu} - 30\Big)$
- discretization of the first order space derivatives $\partial_{xxx}(\cdot)$: $\tilde{\mathrm{T}}^{\mathrm{FD4}} = j\dfrac{k^3}{8\bar{\mu}^3}\Big(-2\sin 3\bar{\mu} + 16\sin 2\bar{\mu} - 26\sin\bar{\mu}\Big)$
- solution of the elliptic problem: $\tilde{\Phi}_{LIN}^{(FD4)} = -\dfrac{gh_0^3}{3}\tilde{\mathrm{T}}^{\mathrm{FD4}}\left(1 - \dfrac{\alpha h_0^2}{3}\tilde{\mathrm{S}}^{\mathrm{FD4}}\right)^{-1}$

Finally, we give in the following the descriptions of the four different configurations studied for the discretization of the elliptic equation (45), whose dispersion errors are compared each other on figures 3, 5 and 7.

1). it stands for the choice to lump both the mass matrices of the equations (8) and (14). The equation (45) thus becomes $\left(1-\frac{\alpha h_0^2}{3}\tilde{\mathrm{S}}^{\mathrm{G}}\right)\phi_i = -\frac{gh_0^3}{3}\tilde{\mathrm{T}}^{\mathrm{G}}\eta_i$ and the related $\tilde{\Phi}_{LIN}$ takes the form:

$$\tilde{\Phi}_{LIN}^{(1)} = -\frac{gh_0^3}{3}\tilde{\mathrm{T}}^{\mathrm{G}}\left(1-\frac{\alpha h_0^2}{3}\tilde{\mathrm{S}}^{\mathrm{G}}\right)^{-1}$$

2). it stands for the choice to lump only the mass matrix of equation (14). The equation (45) thus becomes $\left(\tilde{\mathrm{M}}^{\mathrm{G}}-\frac{\alpha h_0^2}{3}\tilde{\mathrm{S}}^{\mathrm{G}}\right)\phi_i = -\frac{gh_0^3}{3}\tilde{\mathrm{T}}^{\mathrm{G}}\eta_i$ and the related $\tilde{\Phi}_{LIN}$ takes the form:

$$\tilde{\Phi}_{LIN}^{(2)} = -\frac{gh_0^3}{3}\tilde{\mathrm{T}}^{\mathrm{G}}\left(\tilde{\mathrm{M}}^{\mathrm{G}}-\frac{\alpha h_0^2}{3}\tilde{\mathrm{S}}^{\mathrm{G}}\right)^{-1}$$

3). it stands for the choice to lump only the mass matrix of equation (8). The equation (45) thus becomes $\left(1-\frac{\alpha h_0^2}{3}\tilde{\mathrm{S}}^{\mathrm{G}}\right)\phi_i = -\frac{gh_0^3}{3}\tilde{\mathrm{T}}^{\mathrm{G}}\left(\tilde{\mathrm{M}}^{\mathrm{G}}\right)^{-1}\eta_i$ and the related $\tilde{\Phi}_{LIN}$ takes the form:

$$\tilde{\Phi}_{LIN}^{(3)} = -\frac{gh_0^3}{3}\tilde{\mathrm{T}}^{\mathrm{G}}\left(\tilde{\mathrm{M}}^{\mathrm{G}}\right)^{-1}\left(1-\frac{\alpha h_0^2}{3}\tilde{\mathrm{S}}^{\mathrm{G}}\right)^{-1}$$

4). it stands for the choice not to lump any mass matrix. The equation (45) thus dont changes and the related $\tilde{\Phi}_{LIN}$ is given by:

$$\tilde{\Phi}_{LIN}^{(4)} = -\frac{gh_0^3}{3}\tilde{\mathrm{T}}^{\mathrm{G}}\left(\tilde{\mathrm{M}}^{\mathrm{G}}\right)^{-1}\left(\tilde{\mathrm{M}}^{\mathrm{G}}-\frac{\alpha h_0^2}{3}\tilde{\mathrm{S}}^{\mathrm{G}}\right)^{-1}$$

References

[1] J. S. Antunes do Carmo, F. J. Seabra-Santos, and A. B Almeida. Numerical solution of the generalized Serre equations with the maccormack finite-difference scheme. *Int. J. Numer. Meth. Fluids*, 16:725–738, 1993.

[2] P. Bacigaluppi, M. Ricchiuto, and P. Bonneton. A 1d stabilized finite element model for non-hydrostatic wave breaking and run-up. In J. Fuhrmann, M. Ohlberger, and C. Rohde, editors, *Finite Volumes for Complex Applications VII*, volume 77 of *Springer Proceedings in Mathematics and Statistics*. Springer, 2014.

[3] P. Bacigaluppi, M. Ricchiuto, and P. Bonneton. Upwind Stabilized Finite Element Modelling of Non-hydrostatic Wave Breaking and Run-up. Research Report RR-8536, May 2014.

[4] S. Beji and J. A. Battjes. Experimental investigations of wave propagation over a bar. *Coastal Eng.*, 19:151, 1993.

[5] A. Bermudez and M.E. Vazquez. Upwind methods for hyperbolic conservation laws with source terms. *Computers & Fluids*, 23(8):1049 – 1071, 1994.

[6] H. B. Bingham, P. A. Madsen, and D. R. Fuhraman. Velocity potential formulations of highly accurate Boussinesq-type models. *Coastal Engineering*, 56:467, 2009.

[7] P. Bonneton, E. Barthelemy, J. D. Carter, F. Chazel, and S. T. Cien. Fully nonlinear weakly dispersive modelling of wave transformation, breaking and runup. *Preprint submitted to European Journal of Mechanics - B/Fluids*, 2011.

[8] P. Bonneton, F. Chazel, D. Lannes, M. Marche, and M. Tissier. A spliting approach for the fully nonlinear and weakly dispersive green-nagdi model. *J.Comput.Phys*, 230:1479–1498, 2011.

[9] A. G. L. Borthwick, M. Ford, B. P. Weston, P. H. Taylor, and P. K. Stansby. Solitary wave transformation, breaking and run-up at a beach. *Maritime Engineering*, 159:97–105, 2006.

[10] M. Brocchini. A reasoned overview on Boussinesq-type models: the interplay between physics, mathematics and numerics. *Proc.R.Soc.A*, 469:20130496, 2013.

[11] P. Brufau, P. García-Navarro, and M. E. Vázquez-Cendón. Zero mass error using unsteady wetting-drying coditions in shallow flows over dry irregular topography. *Int. J. Numer. Meth. Fluids*, 45:1047–1082, 2004.

[12] P. Brufau, M. E. Vázquez-Cendón, and P. Gracía-Navarro. A numerical model for the flooding and drying of irregular domains. *Int. J. Numer. Meth. Fluids*, 39:247–275, 2002.

[13] M. J. Castro, A. M. Ferreiro, J. A. García-Rodriguez, J. M. González-Vida, J. Macías, C. Parés, and M. E. Vázquez-Cendón. The numerical treatment of wet/dry fronts in shallow flows: Application to one-layer and two-layer systems. *Mathematical and Computer Modelling*, 42:419–439, 2005.

[14] F. Chazel, D. Lannes, and F Marche. Numerical Simulation of Strongly Nonlinear and Dispersive Waves Using a Green-Naghdi Model. *J. Sci. Comput.*, 48:105–116, 2011.

[15] R. Cienfuegos, E. Barthélemy, and P. Bonneton. A fourth-order compact finite volume scheme for fully nonlinear and weakly dispersive Boussinesq-type equations. Part I: Model development and analysis. *Int. J. Numer. Methods Fluids*, 51:1217–1253, 2006.

[16] R. Cienfuegos, E. Barthélemy, and P. Bonneton. A fourth-order compact finite volume scheme for fully nonlinear and weakly dispersive Boussinesq-type equations. Part II: Boundary conditions and validation. *Int. J. Numer. Methods Fluids*, 53:1423–1455, 2007.

[17] R. Cienfuegos, E. Barthélemy, and P. Bonneton. Wave-breaking model for Boussinesq-type equations including roller effects in the mass conservation equation. *J. Waterw., Port, Coast., Ocean Engrg.*, 136:10–26, 2010.

[18] A. I. Delis, I. K. Nikolos, and M. Kazolea. Performance and comparison of cell-centered and node-centered unstructured finite volume discretizations for shallow water free surface flows. *Archives of Computational Methods in Engineering*, 18:57–118, 2011.

[19] S. Gottlieb, C.-W. Shu, and E. Tadmor. *SIAM Review*, (1):89–112, 2001.

[20] A. E. Green and P. M. Nagdi. A derivation of equations for wave propagation in water of variable depth. *J. Fluid Mech.*, 78:237–246, 1976.

[21] M. E. Hubbard and P. García-Navarro. Flux difference splitting and the balancing of source terms and flux gradients. *J. Comp. Phys.*, 165:89–125, 2000.

[22] T.J.R. Hughes, G. Scovazzi, and T. Tezduyar. Stabilized methods for compressible flows. *J. Sci. Comp.*, 43:343–368, 2010.

[23] W. Hundsdorfer, S. J. Ruuth, and R. J. Spiteri. Monotonicity-preserving linear multistep methods. *SIAM Journal on Numerical Analysis*, 41:605–623, 2003.

[24] M. Kazolea and A. I. Delis. A well-balanced shock-capturing hybrid finite volume-finite difference numerical scheme for extended 1D boussinesq models. *Applied Numerical Mathematics*, 67:167–186, 2013.

[25] M. Kazolea, A. I. Delis, and C. E. Synolakis. Numerical treatment of wave breaking on unstructured finite volume approximations for extended Boussinesq-type equations. *J. Comp. Phys.*, 271:281–305, 2014.

[26] M. J. Kermani, A. G. Geber, and J. M. Stockie. Thermodynamically based moisture prediction using Roe's scheme. In *The 4th Conference of Iranian AeroSpace Society*, 2003. Amir Kabir University of Technology, Tehran, Iran, January.

[27] J. Klosa. Extrapolated BDF residual distribution schemes for the shallow water equations. Master thesis, 2012.

[28] D. Lannes and P. Bonneton. Derivation of asymptotic two-dimensional time-dependent equations for surface water wave propagation. *Phys. Fluids*, 21, 2009.

[29] R. J. LeVeque. *Finite Volume Methods for Hyperbolic Problems*. Cambridge University Press, 2002.

[30] M. Li, P. Guyenne, F. Li, and L. Xu. Highorder well-balanced CDG-FE methods for shallow water waves by a Green-Naghdi model. *J.Comput.Phys.*, 257:169–192, 2014.

[31] Q. Liang and A. G. L. Borthwick. Adaptive quadtree simulation of shallow flows with wet/dry front over complex topography. *Comput. Fluids*, 38:221–234, 2009.

[32] P. J. Lynett. Nearshore Wave Modeling with High-Order Boussinesq-Type Equations. *Journal of Waterway, Port, Coastal, and Ocean Engineering*, 132:348–357, 2006.

[33] P. A. Madsen and H. A. Schäffer. Higher-order Boussinesq-type equations for surface gravity waves: derivation and analysis. *Philos. Trans. R. Soc. Lond.*, 356:3123–3184, 1998.

[34] P. A. Madsen and O. R. Sørensen. A new form of the Boussinesq equations with improved linear dispersion characteristics. Part 2: A slowing varying bathymetry. *Coast. Eng.*, 18:183–204, 1992.

[35] F. Marche and D. Lannes. A new class of fully nonlinear and weakly dispersive green-nagdi models for efficient 2d simulations. *sumbitted to J. Comp. Phys.*, 2015.

[36] D. E. Mitsotakis, B. Ilan, and D. Dutykh. On the Galerkin/finite-element method for the Serre equations. *J. Sci. Comp.*, 61:166–215, 2014.

[37] J. Murillo, P. Garcia-Navarro, and J. Burguete. Time step restrictions for well-balanced shallow water solutions in non-zero velocity steady states. *Int. J. for Num. Meth. Fluids*, 60:1351, 2009.

[38] J. Murillo, P. Garcia-Navarro, J. Burguete, and P. Brufau. The influence of source terms on stability, accuracy and conservation in two-dimensional shallow flow simulation using triangular finite volumes. *Int. J. for Numer. Methods in Fluids*, 54:543, 2007.

[39] I. K. Nikolos and A. I. Delis. An unstructured node-centered finite volume scheme for shallow water flows with wet/dry fronts over complex topography. *Comput. Methods Appl. Mech. Engrg*, 198:3723–3750, 2009.

[40] O. Nwogu. An alternative form of the Boussinesq equations for nearshore wave propagation. *Journal of Waterway, Port, Coastal, and Ocean Engineering*, 119:618–638, 1994.

[41] J. Orszaghova, A. G. L. Borthwick, and P. H. Taylor. From the paddle to the beach - A Boussinesq shallow water numerical wave tank based on Madsen, and Sørensen's equations. *J. Comp. Phys.*, 231:328–344, 2012.

[42] M Ricchiuto. An explicit residual based approach for shallow water flows. *J. Comp. Phys.*, 280:306–304, 2015.

[43] M. Ricchiuto and A. Bollermann. Stabilized residual distribution for shallow water simulations. *J. Comp. Phys.*, 228:1071–1115, 2009.

[44] M. Ricchiuto and A.G. Filippini. Upwind residual discretization of enhanced boussinesq equations for wave propagation over complex bathymerties. *J. Comput. Phys.*, 271:306–341, 2014.

[45] P. L. Roe. Approximate Riemann solvers, parameter vectors, and difference schemes. *J. Comp. Phys.*, 43:357–372, 1981.

[46] V. Roeber, K. F. Cheung, and M. H. Kobayashi. Shock-capturing Boussinesq-type model for nearshore wave processes. *Coast. Eng.*, 57:407–423, 2010.

[47] V. Roeber and K.F. Cheung. Boussinesq-type model for energetic breaking waves in fringing reef environment. *Coast. Eng.*, 70:1–20, 2012.

[48] H. A. Schäffer, P.A. Madsen, and R. Deigaard. A Boussinesq model for waves breaking in shallow water. *Coast. Eng.*, 20:185–202, 1993.

[49] F. J. Sebra-Santos, D. P. Renouard, and A. M Temperville. Numerical and experimental study of the transformation of a solitary wave over a self or isolated obstacle. *J. Fluid Mech.*, 185:523–545, 1987.

[50] F. Shi, J. T. Kirby, J. C. Harris, J. D. Geiman, and S. T. Grilli. A high-order adaptive time-stepping tvd solver for boussinesq modeling of breaking waves and coastal inundation. *Ocean Modelling*, 43-44:36–51, 2012.

[51] O. R. Sørensen, H. A. Schäffer, and P. A. Madsen. Surf zone dynamics simulated by a Boussinesq type model: Part III. Wave-induced horizontal nearshore circulations. *Coastal. Eng.*, 33:155–176, 1998.

[52] C. E. Synolakis. The run up of solitary waves. *J. Fluid Mech.*, 185:532–545, 1987.

[53] C. E. Synolakis, E. N. Bernard, V. V. Titov, U. Kanoglu, and F. I. Gonzalez. Standards, criteria, and procedures for NOAA evaluation of tsunami numerical models. NOAA Tech. Memo. OAR PMEL-135, NOAA/Pacific Marine Environmental Laboratory, Seattle, WA, 2007.

[54] M. Tissier, P. Bonneton, F. Marche, F. Chazel, and D. Lannes. A new approach to handle wave breaking in fully non-linear Boussinesq models. *Coastal Engineering*, 67:54–66, 2012.

[55] M. Tonelli and M. Petti. Hybrid finite-volume finite-difference scheme for 2DH improved Boussinesq equations. *Coast. Eng.*, 56:609–620, 2009.

[56] M. Tonelli and M. Petti. Finite volume scheme for the solution of 2D extended Boussinesq equations in the surf zone. *Ocean. Eng.*, 37:567–582, 2010.

[57] M. Tonelli and M. Petti. Shock-capaturing Boussinesq model for irregular wave propagation. *Coastal Engineering*, 61:8–19, 2012.

[58] M. Walkey and M. Berzins. A finite element method for the two-dimensional extended Boussinesq equations. *Int. J. Numer. Meth. Fluids*, 39:865, 2002.

[59] N.P. Waterson and H. Deconinck. Design principles for bounded higher-order convection schemes ? a unified approach. *J.Comput.Phys.*, 224(1):182 – 207, 2007.

[60] G. Wei and J. T. Kirby. A time-dependent numerical code for extended Boussinesq equations. *Journal of Waterway, Port, Coastal, and Ocsean Engineering*, 120:251–261, 1995.

[61] G. Wei, J. T. Kirby, S. T. Grilli, and Subramanya. A fully nonlinear Boussinesq model for surface waves. Part 1. Highly nonlinear unsteady waves,. *J. Fluid Mech.*, 294:71, 1995.

[62] G. Wei, J. T. Kirby, and A. Sinha. Generation of waves in Boussinesq models using a source function approach. *Coastal Eng.*, 36:271, 1999.

[63] Y. Xing, X. Zhang, and C.-W. Shu. Positivity-preserving high order well-balanced discontinuous galerkin methods for the shallow water equations. *Advances in Water Resources*, 33(12):1476 – 1493, 2010.

[64] X. Zhang, Y. Xia, and C.-W. Shu. Maximum-principle-satisfying and positivity-preserving high order discontinuous galerkin schemes for conservation laws on triangular meshes. *Journal of Scientific Computing*, (50):29–62, 2012.

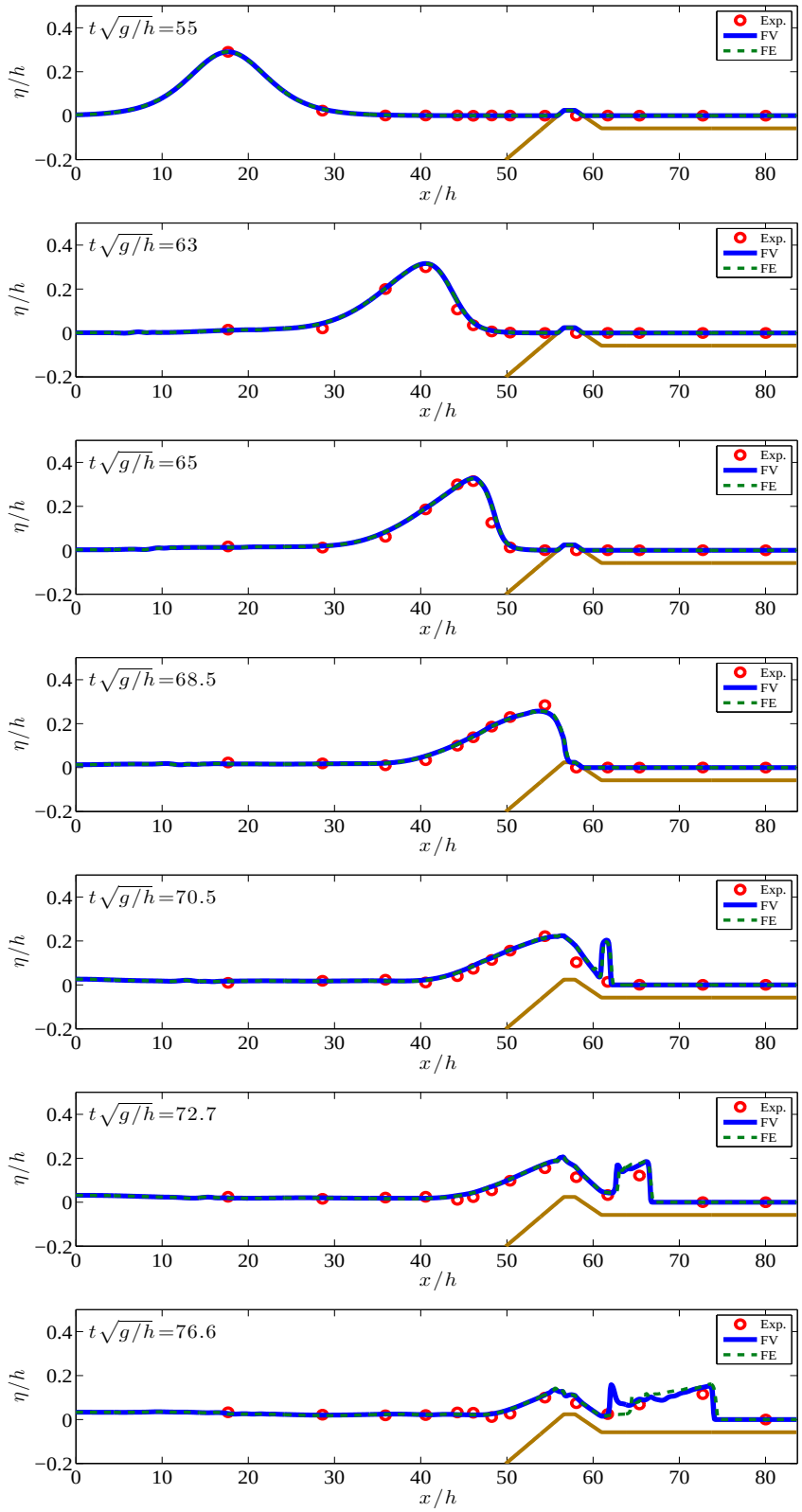

Figure 23: Evolution of surface profiles and wave transformations over an exposed reef for $A/h = 0.3$ and $1/12$ slope

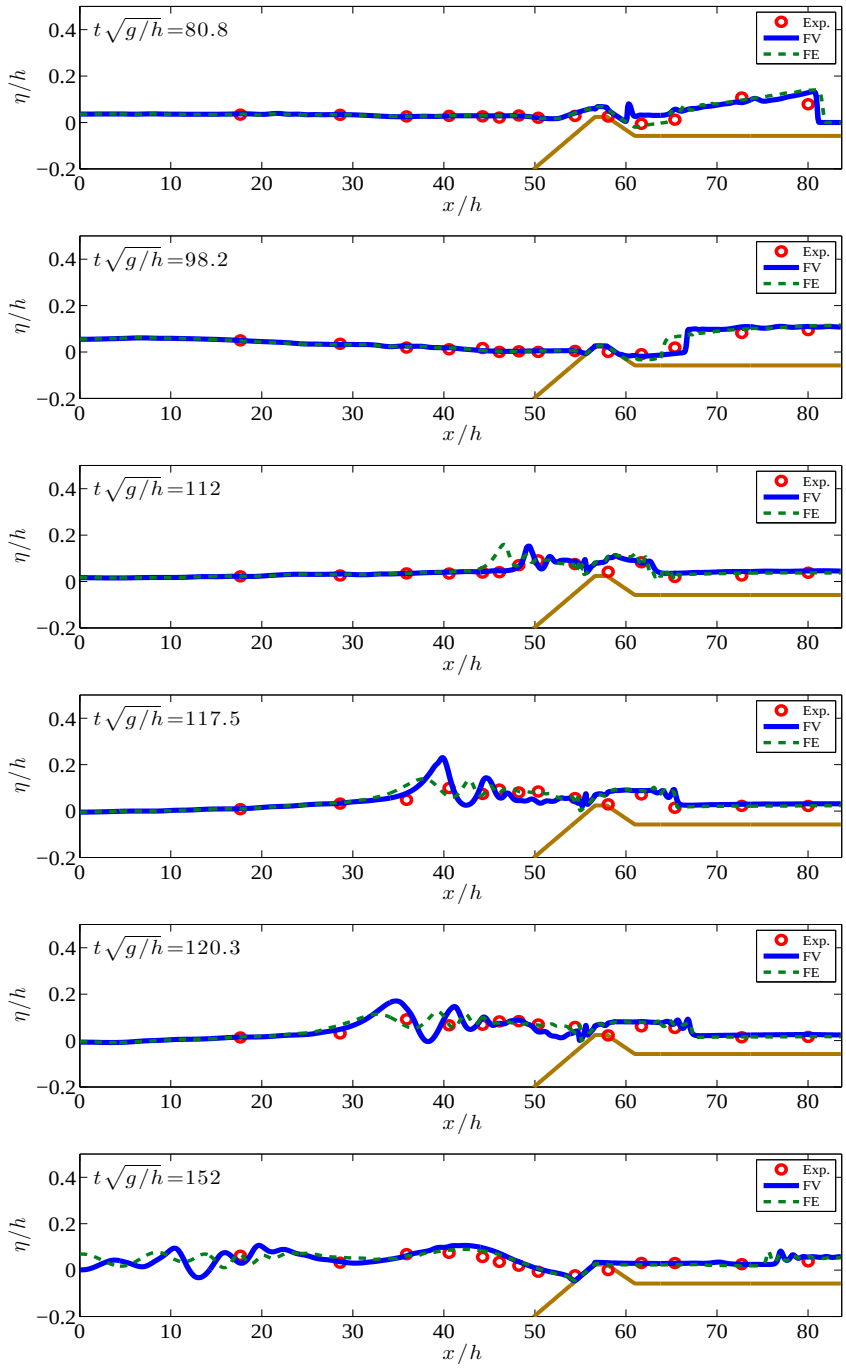

Figure 24: Evolution of surface profiles and wave transformations over an exposed reef for $A/h = 0.3$ and $1/12$ slope

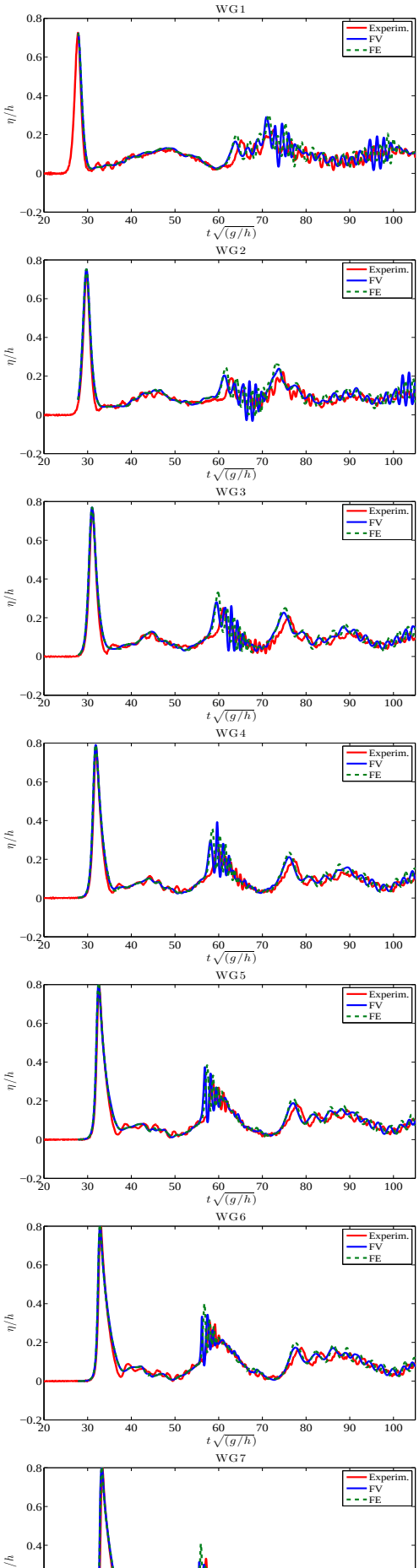
WG1
WG2
WG3
WG4
WG5
WG6
WG7
Experim.
FV
FE
η/h
$t\sqrt{(g/h)}$

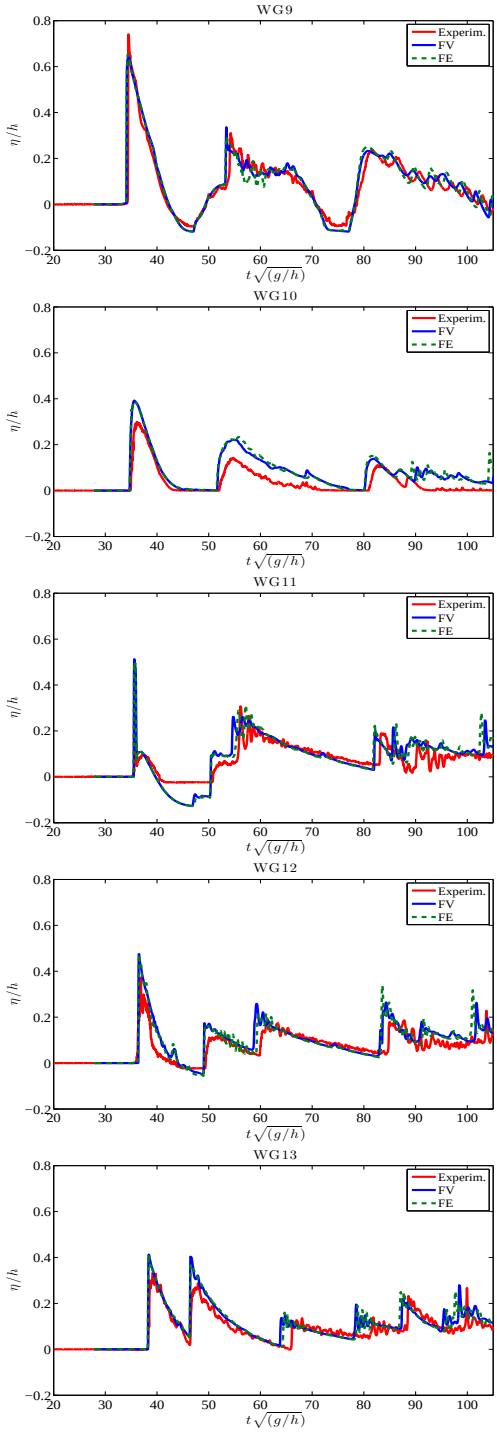

Figure 26: Time series of the normalized free surface at the wave gauges on top and after the reef

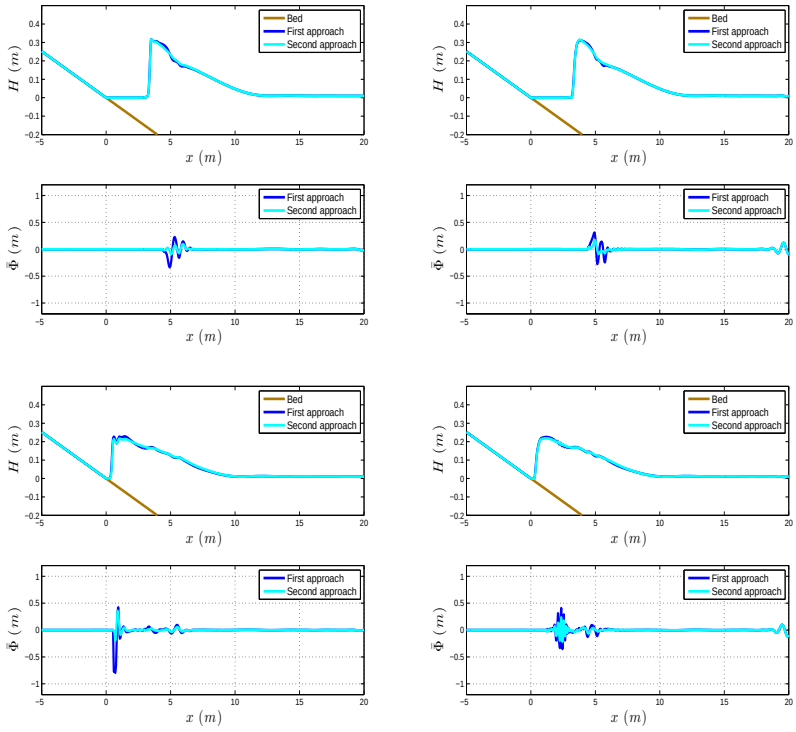

Figure 27: Surface elevation and $\bar{\mathbf{\Phi}}$ for FV and SUPG scheme for a solitary wave of $\epsilon = 0.28$.

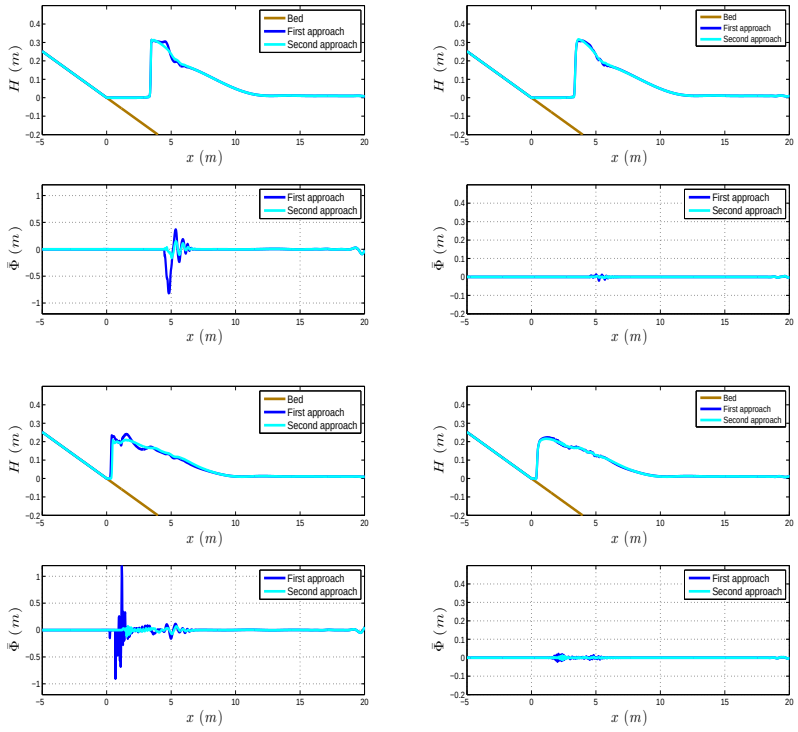

Figure 28: Surface elevation and $\bar{\mathbf{\Phi}}$ for FV and SUPG scheme for a solitary wave of $\epsilon = 0.28$ and a refined mesh

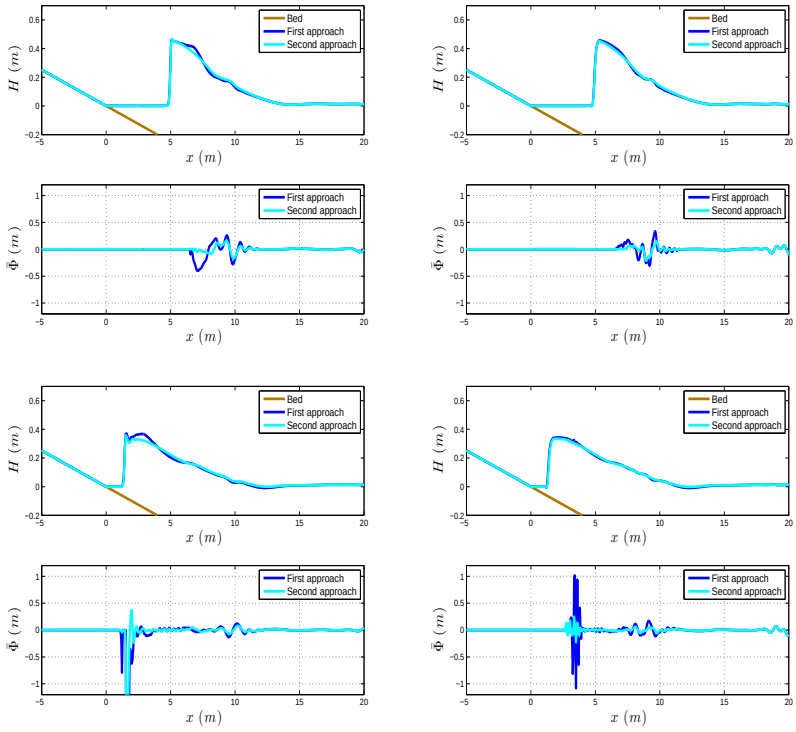

Figure 29: Surface elevation and $\bar{\mathbf{\Phi}}$ for FV and SUPG scheme for a solitary wave of $\epsilon = 0.5$.

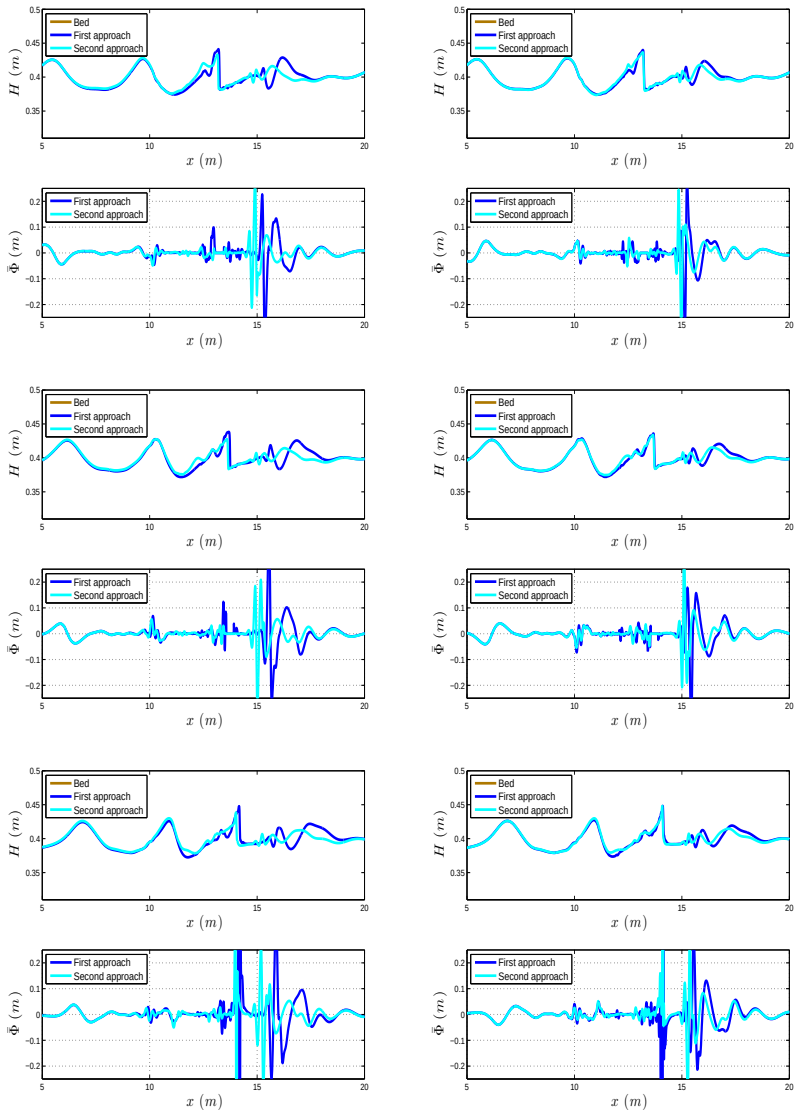

Figure 30: Surface elevation and $\bar{\mathbf{\Phi}}$ for FV and SUPG scheme for a solitary wave over a bar.

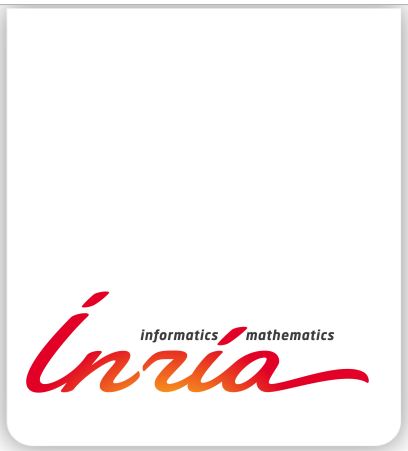

RESEARCH CENTRE
BORDEAUX – SUD-OUEST

351, Cours de la Libération
Bâtiment A 29
33405 Talence Cedex

Publisher
Inria
Domaine de Voluceau - Rocquencourt
BP 105 - 78153 Le Chesnay Cedex
inria.fr

ISSN 0249-6399